

Supporting Information

**Crystalline Mixed-Valence Copper Supramolecular Isomer for
Electroreduction of CO₂ to Hydrocarbons**

Jia-Ni Lu,^a Jiang Liu,*^a Lei Zhang,^a Long-Zhang Dong,^a Shun-Li Li,^{*a} and Ya-Qian Lan^{*ab}

^a Jiangsu Collaborative Innovation Centre of Biomedical Functional Materials, School of Chemistry and Materials Science, Nanjing Normal University, Nanjing, 210023 (China)

^b School of Chemistry, South China Normal University, Guangzhou, 510006 (China)

*Corresponding Author(s): J. L. (E-mail: liuj@njnu.edu.cn)

S.-L. L.(E-mail: slli@njnu.edu.cn)

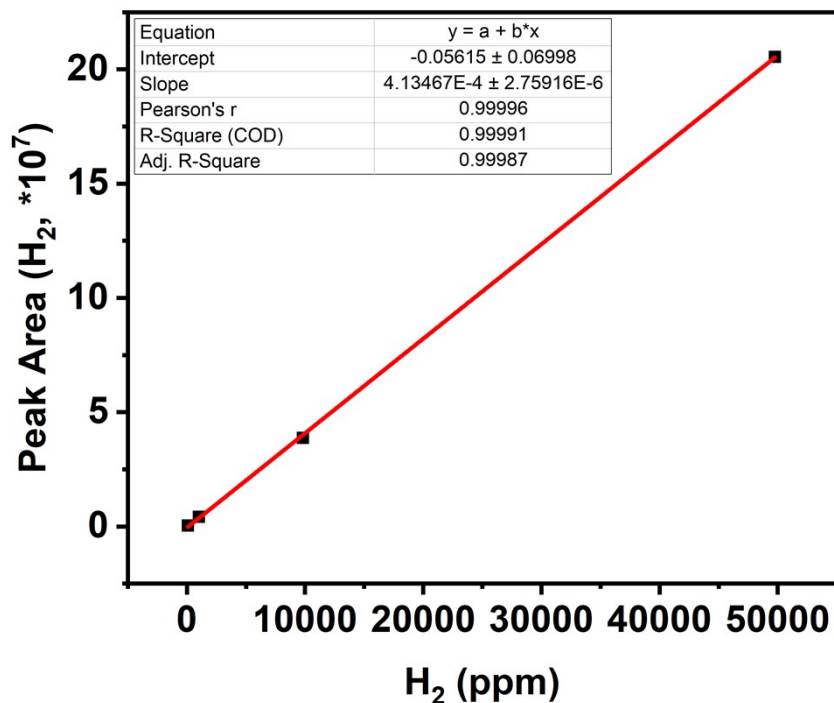
Y.-Q. L. (E-mail: yqlan@m.scnu.edu.cn; yqlan@njnu.edu.cn;

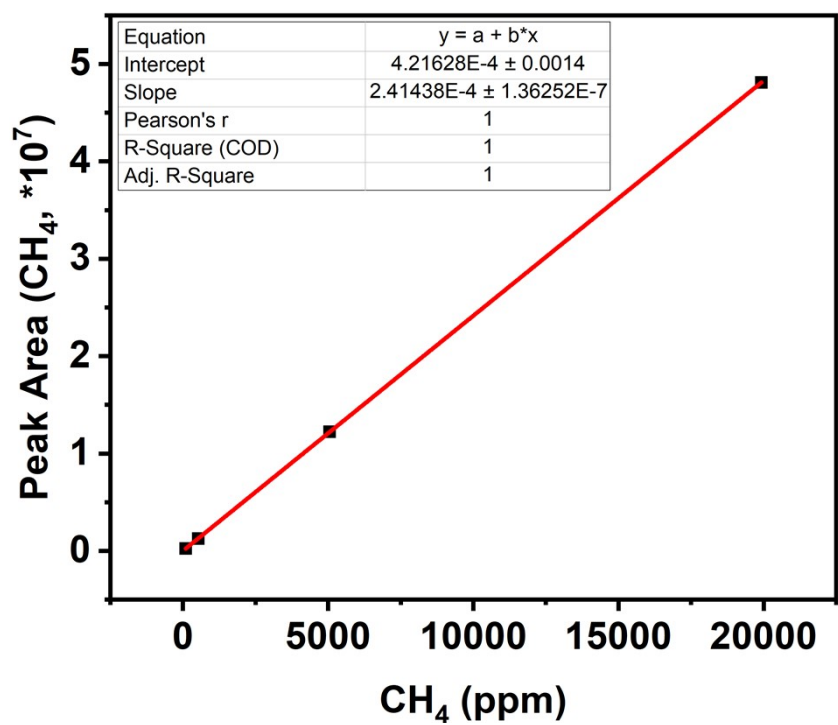
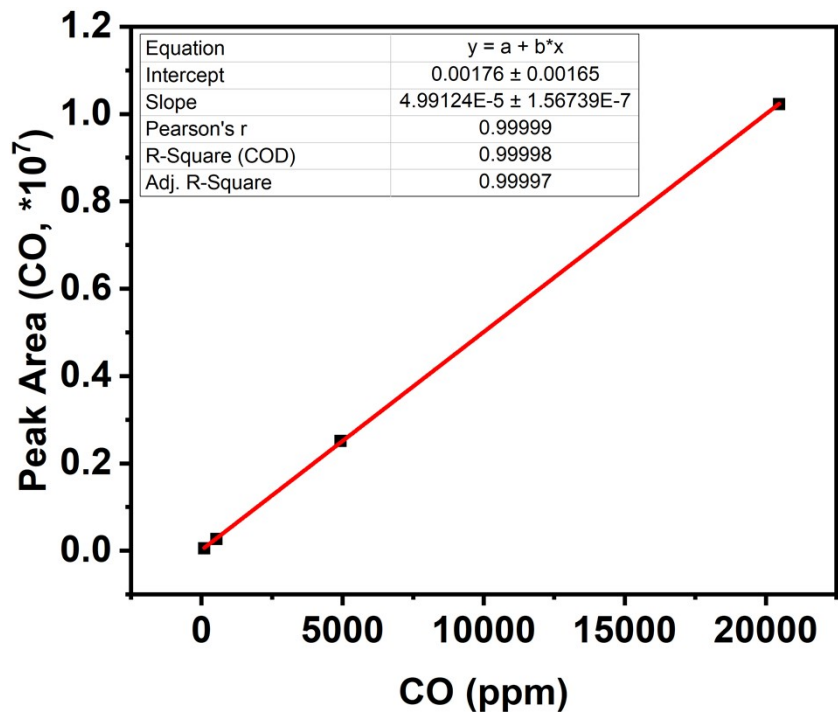
Homepage: <http://www.yqlangroup.com>)

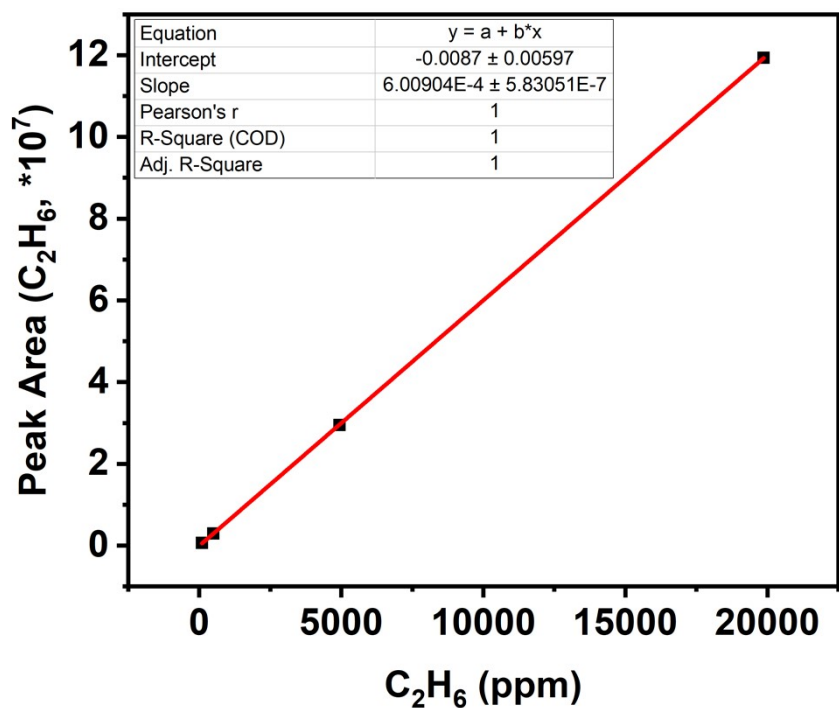
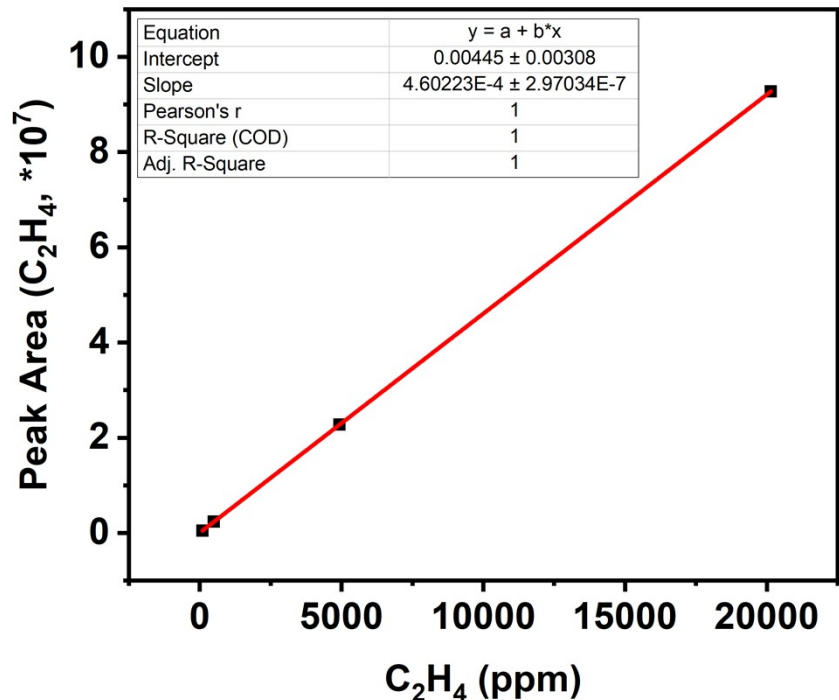
Standard Curves on GC

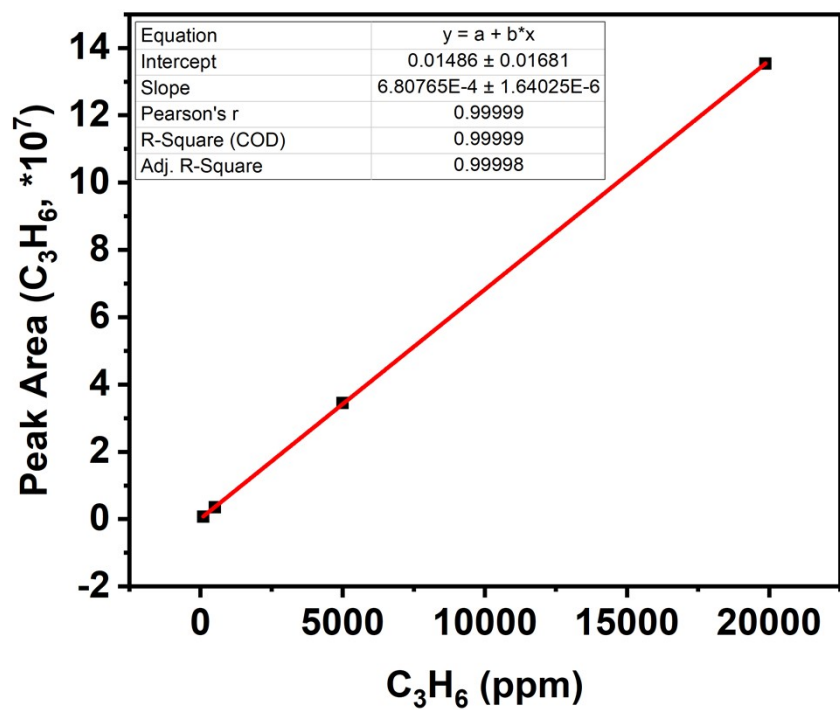
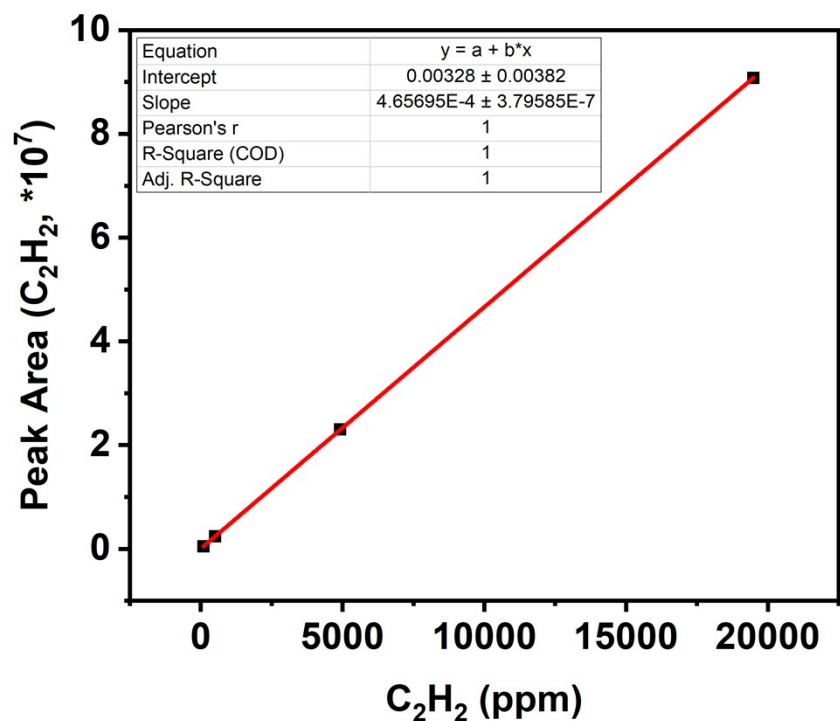
Four concentrations of standard mixed gases (1~4) contained H₂, CO, CH₄, C₂H₂, C₂H₄, C₂H₆, C₃H₆, and C₃H₈ with CO₂ balance were used to calculate the standard curves for GC measurements. The concentration of the components (ppm) and the final standard curves are listed below.

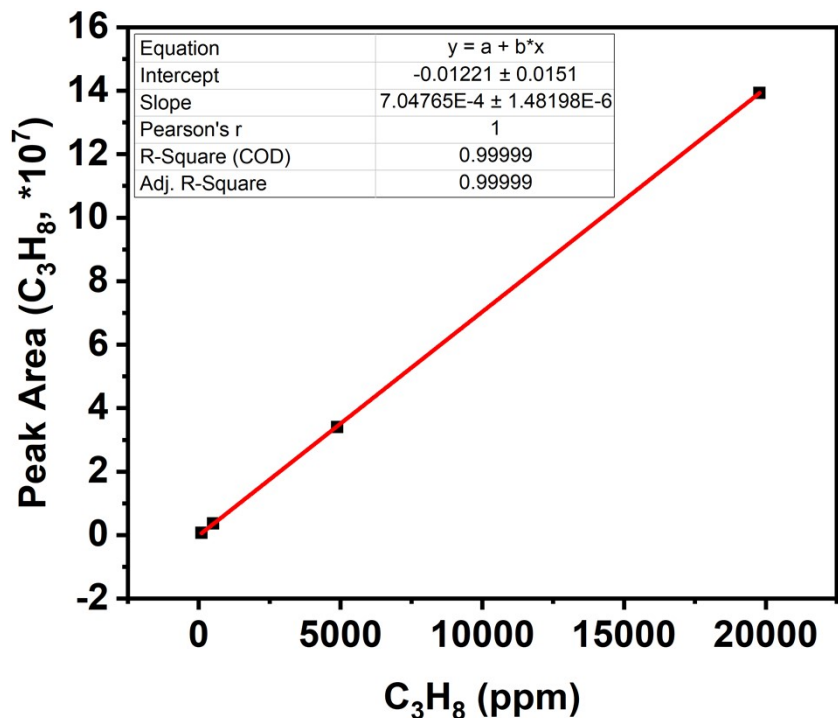
	1	2	3	4
H ₂	99.40	1010.30	9821.20	49757.50
CO	99.10	527.60	4936.20	20464.40
CH ₄	100.50	529.10	5059.50	19919.10
C ₂ H ₄	99.50	502.70	4928.50	20143.00
C ₂ H ₆	101.80	504.10	4941.40	19870.40
C ₂ H ₂	99.90	514.80	4913.80	19492.00
C ₃ H ₆	98.20	515.00	5002.20	19870.90
C ₃ H ₈	99.20	515.40	4882.70	19774.80



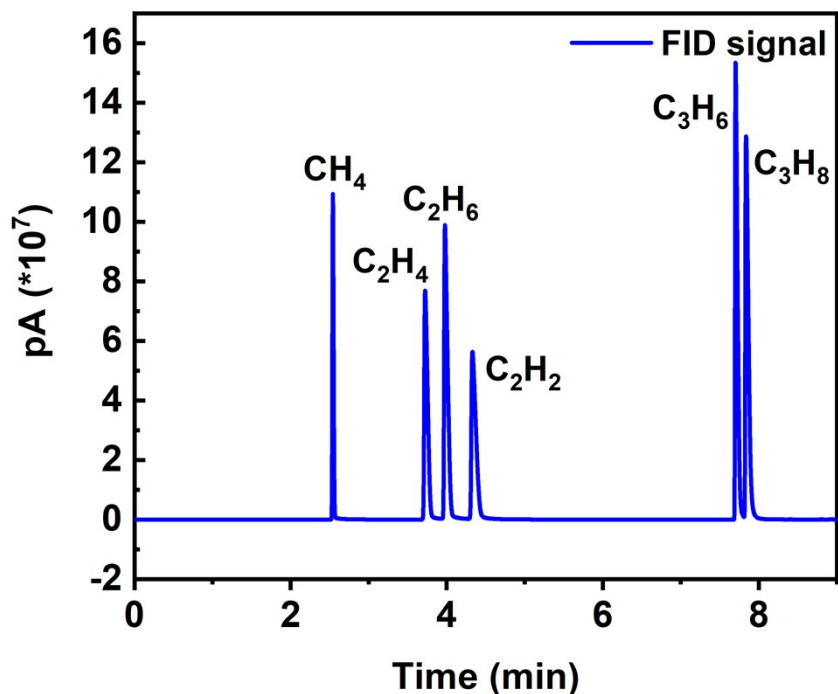


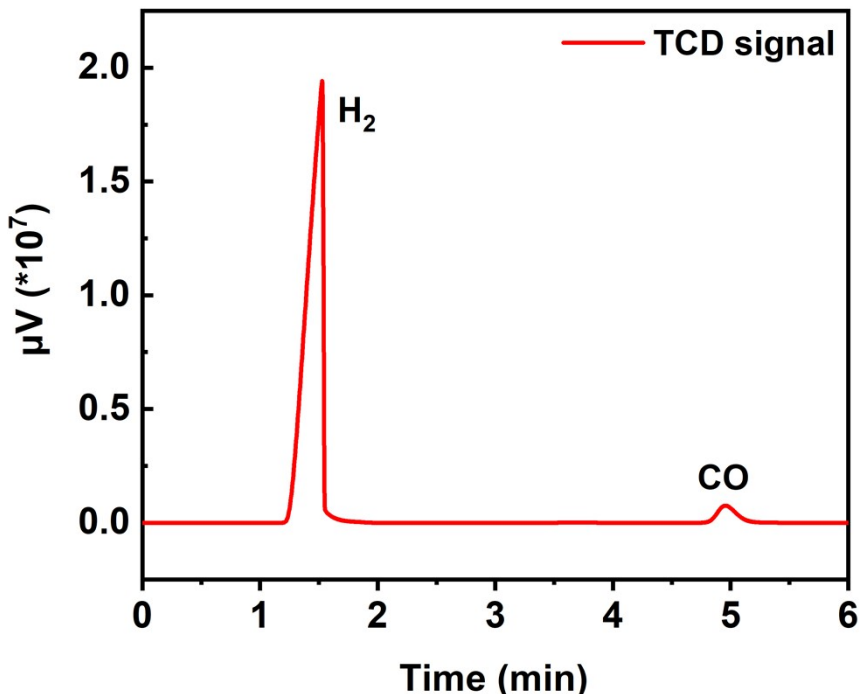






The standard curves of H₂, CO, CH₄, C₂H₄, C₂H₆, C₂H₂, C₃H₆, and C₃H₈. H₂ and CO are detected by TCD and all the hydrocarbons are detected by FID. High linearities ensure the reliability of our data.





The gas chromatogram of FID (blue) and TCD (green) show that all the tested substance can be completely baseline separated.

Partial current density calculation

Partial current density ($j_{product}$) of each product was calculated as follows:

$$j_{product} = j_{total} \times FE_{product}$$

where j_{total} is the average total current density (mA cm^{-2}) during electrolysis.

Turnover frequency calculation

Turnover frequency (TOF) values for CH_4 were calculated according to the following equation:

$$\text{TOF} = \frac{j_{\text{CH}_4}/NF}{m_{\text{cat}} \times \omega/M_{\text{Cu}}} \times 3600$$

j_{CH_4} is partial current for certain product, CH_4 ; N is the number of electron transferred for product formation, which is 8 for CH_4 ; F is Faradaic constant, 96485 C mol^{-1} ; m_{cat} is catalyst mass in the electrode, g; ω is Cu(I) loading in the catalyst; M_{Cu} is atomic mass of Cu, $63.456 \text{ g mol}^{-1}$.

Isotopic labeling control experiment

In isotope experiments, $^{13}\text{CO}_2$ was employed to confirm the carbon source of CH_4 , C_2H_4 , and CO formed by electrocatalytic CO_2 reduction. The $^{13}\text{CH}_4$, $^{13}\text{C}_2\text{H}_4$, and ^{13}CO were analyzed using gas GC-MS.

Computational details

In this work, we chose the single-layer structure of **CuL-2**, **CuL-3**, and **CuL-4** as the computational model to compare the thermodynamic stability. Additionally, the **CuL-4** was chosen as the computational model to reveal the role of Cu(I) and Cu(II) catalytic sites in the CO₂RR process. All the calculations are performed within the framework of DFT implemented in the Vienna ab initio simulation package (VASP).¹⁻³ The generalized gradient approximation with the functional is described by the Perdew-Burke-Ernzerhof type (PBE).⁴ The projector-augmented wave (PAW) method⁵ is applied to describe the wavefunctions in the core regions, while the valence wavefunctions are expanded as linear combination of plane-waves with a cutoff energy of 400 eV. The total energy is converged to 10⁻⁵ eV in the geometry optimizations, and the Hellmann-Feynman force on each relaxed atom is less than 0.02 eV/Å. To simulate a charged cell with applied potentials in the experiments, the negative charge is added to the system and the compensating charge is placed in the electrolyte which is approximated by a polarizable dielectric continuum (i.e., an implicit solvation model) with VASPsol^{6,7}. The applied potential of -1.0 V is obtained by the shift of the work function as used in previous studies⁸.

Gibbs reaction free energy of reaction for CO₂RR elementary steps involving (H⁺ + e⁻) pair transfer was calculated using computational hydrogen electrode (CHE) model⁹. At U=0 V, $\Delta G = \Delta E + \Delta E_{ZPE} - T\Delta S + \int C_p dT$, where ΔE is the reaction energy difference between the product and reactant of the CO₂RR occurring on catalysts, which can be directly obtained from DFT computations; ΔE_{ZPE} , $T\Delta S$ and $\int C_p dT$ are zero-point energy correction, entropy correction and enthalpic temperature correction at T=298.15 K respectively, which were calculated from the vibrational frequencies.

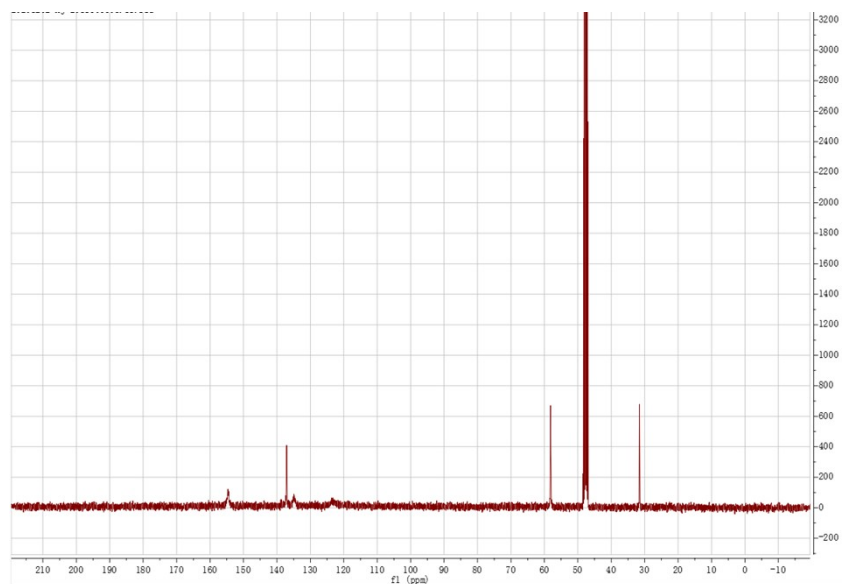


Fig. S1 ¹³C NMR spectrum for the ligand H₂L.

Table S1. Crystal data and structure refinement of CuL-1, CuL-2, CuL-3, and CuL-4.

Complexes	CuL-1	CuL-2	CuL-3	CuL-4
formula	$C_{33}H_{36}Cu_6N_{21}O_9$	$C_{23}H_{30}ClCu_3N_{12}O_2$	$C_{22}H_{24}Cl_2Cu_4N_{12}$	$C_{22}H_{24}ClCu_3N_{12}$
formula weight	1252.07	732.66	781.59	682.65
crystal system	triclinic	orthorhombic	monoclinic	monoclinic
space group	<i>P</i> -1	<i>Pnma</i>	<i>C2/c</i>	<i>P21/c</i>
<i>a</i> (Å)	9.6945(1)	14.571(4)	24.259(5)	11.806(4)
<i>b</i> (Å)	14.397(2)	21.305(6)	9.6320(1)	9.525(3)
<i>c</i> (Å)	17.330(2)	9.400(3)	14.083(3)	14.533(4)
α (°)	106.769(2)	90	90	90
β (°)	96.711(2)	90	120.379(5)	97.871(9)
γ (°)	106.277(2)	90	90	90
<i>V</i> (Å ³)	2171.0(5)	2918.1(1)	2838.8(9)	1618.7(8)
<i>Z</i>	2	4	4	2
<i>D_{calc}</i> (g·cm ⁻³)	1.915	1.668	1.829	1.328
<i>R_{int}</i>	0.0161	0.0536	/	0.0651
μ (mm ⁻¹)	2.965	2.303	3.182	1.982
<i>F</i> (000)	1254	1488	1560	654
<i>R</i> ₁ [$ I > 2\sigma(I)$] ^a	0.0307	0.0756	0.0434	0.0857
<i>wR</i> ₂ [$ I > 2\sigma(I)$] ^b	0.0797	0.1372	0.0943	0.1604
<i>R</i> ₁ (all data)	0.0401	0.1152	0.0741	0.1653
<i>wR</i> ₂ (all data)	0.0847	0.1568	0.1047	0.1967
GOF on <i>F</i> ²	1.024	1.168	1.046	1.105

^a $R_1 = \sum ||F_o|| - |F_c| | / \sum |F_o|$. ^b $wR_2 = |\sum w(|F_o|^2 - |F_c|^2)| / \sum |w(F_o^2)|^{1/2}$

Table S2 Selected bond distance (Å) of **CuL-1**.

Atom1	Atom2	Length/Å
Cu6	N17	1.982(2)
Cu6	N14	1.993(2)
Cu6	N15	2.003(2)
Cu6	O7	2.412(3)
Cu6	N16	2.000(2)
Cu2	N2	1.995(2)
Cu2	N4	2.024(2)
Cu2	N3	1.987(2)
Cu2	N5	1.969(2)
Cu2	O1	2.404(3)
Cu4	N8	1.970(2)
Cu4	N10	2.009(2)
Cu4	N9	2.003(2)
Cu4	N11	1.979(2)
Cu4	O4	2.356(3)
Cu1	N18	1.858(2)
Cu1	N1	1.859(2)
Cu3	N7	1.860(2)
Cu3	N6	1.861(2)
Cu5	N13	1.857(2)
Cu5	N12	1.860(2)

Table S3 Selected bond distance (Å) of **CuL-2**.

Atom1	Atom2	Length/Å
Cu2	N5	2.009(3)
Cu2	N4	2.018(3)
Cu2	N2	2.017(3)
Cu2	N6 ¹	2.228(3)
Cu2	N3	2.025(4)
Cu1	N1	1.862(4)
Cu1	N1 ²	1.862(4)
Cu3	Cl1	2.0856(19)
Cu3	Cl1 ³	2.0856(19)

Table S4 Selected bond distance (Å) of **CuL-3**.

Atom1	Atom2	Length/Å
Cu01	N4	2.015(6)
Cu01	N2	1.994(6)
Cu01	N3	2.027(6)
Cu01	N5	1.984(6)
Cu01	N6 ¹	2.210(6)
Cu02	N1 ²	1.870(6)
Cu02	N1	1.870(6)

Table S5 Selected bond distance (Å) of **CuL-4**.

Atom1	Atom2	Length/Å
Cu2	N5	2.000(6)
Cu2	N6 ¹	2.175(6)
Cu2	N3	2.029(7)
Cu2	N2	1.985(7)
Cu2	N4	2.003(7)
Cu1	N1	1.896(9)
Cu1	N1 ²	1.896(9)

Table S6 Selected bond angles ($^{\circ}$) of CuL-1.

Atom1	Atom2	Atom3	Angle/ $^{\circ}$
N17	Cu6	N14	100.72(9)
N17	Cu6	N15	169.19(10)
N17	Cu6	O7	98.90(9)
N17	Cu6	N16	82.21(9)
N14	Cu6	N15	82.99(9)
N14	Cu6	O7	97.79(9)
N14	Cu6	N16	166.85(10)
N15	Cu6	O7	90.58(9)
N16	Cu6	N15	91.96(9)
N16	Cu6	O7	94.39(9)
N2	Cu2	N4	159.02(10)
N2	Cu2	O1	94.72(9)
N4	Cu2	O1	105.61(9)
N3	Cu2	N2	82.45(9)
N3	Cu2	N4	91.21(9)
N3	Cu2	O1	93.01(9)
N5	Cu2	N2	100.64(9)
N5	Cu2	N4	82.47(9)
N16	Cu6	O7	94.39(9)
N2	Cu2	N4	159.02(10)
N2	Cu2	O1	94.72(9)
N4	Cu2	O1	105.61(9)
N3	Cu2	N2	82.45(9)
N3	Cu2	N4	91.21(9)
N3	Cu2	O1	93.01(9)
N5	Cu2	N2	100.64(9)
N5	Cu2	N4	82.47(9)

Table S7 Selected bond angles ($^{\circ}$) of **CuL-2**.

Atom1	Atom2	Atom3	Angle/ $^{\circ}$
N5	Cu2	N4	82.23(13)
N5	Cu2	N2	101.83(13)
N5	Cu2	N6 ¹	97.94(13)
N5	Cu2	N3	164.20(15)
N4	Cu2	N6 ¹	99.91(14)
N4	Cu2	N3	90.46(14)
N2	Cu2	N4	164.07(14)
N2	Cu2	N6 ¹	94.81(12)
N2	Cu2	N3	81.65(14)
N3	Cu2	N6 ¹	97.10(15)
N1 ²	Cu1	N1	175.3(2)
Cl1	Cu3	Cl1 ³	180.0

Table S8 Selected bond angles ($^{\circ}$) of **CuL-3**.

Atom1	Atom2	Atom3	Angle/ $^{\circ}$
N4	Cu01	N3	92.4(3)
N4	Cu01	N6 ¹	98.5(2)
N2	Cu01	N4	167.2(2)
N2	Cu01	N3	81.6(2)
N2	Cu01	N61	93.3(2)
N3	Cu01	N61	96.0(2)
N5	Cu01	N4	81.8(2)
N5	Cu01	N2	101.7(2)
N5	Cu01	N3	166.6(2)
N5	Cu01	N61	96.8(2)
N12	Cu02	N1	163.4(4)

Table S9 Selected bond angles ($^{\circ}$) of CuL-4.

Atom1	Atom2	Atom3	Angle/ $^{\circ}$
N5	Cu2	N6 ¹	100.9(2)
N5	Cu2	N3	157.7(3)
N5	Cu2	N4	81.3(3)
N3	Cu2	N6 ¹	101.1(3)
N2	Cu2	N5	100.1(3)
N2	Cu2	N6 ¹	97.2(3)
N2	Cu2	N3	81.3(3)
N2	Cu2	N4	165.1(3)
N4	Cu2	N6 ¹	97.1(3)
N4	Cu2	N3	91.8(3)
N1 ²	Cu1	N1	180.0(5)

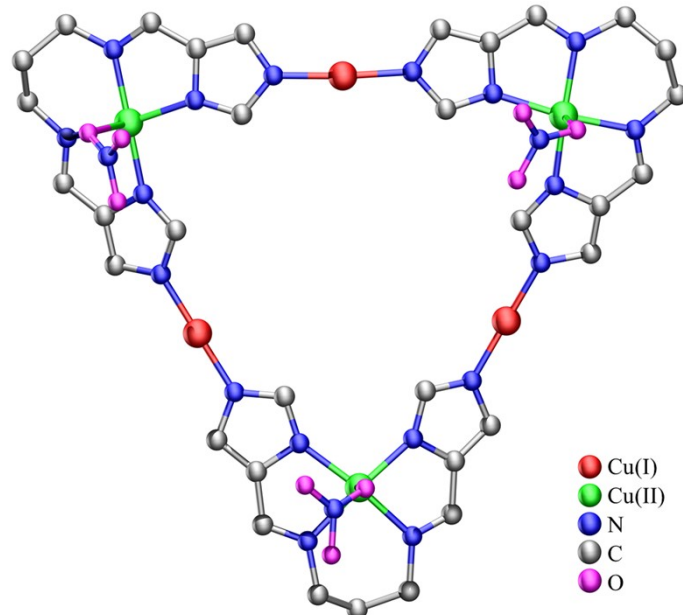


Fig. S2 The asymmetric unit of **CuL-1**. All hydrogen atoms are omitted for clarity.

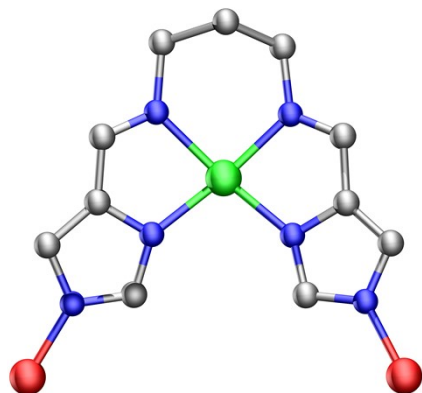


Fig. S3 The coordination environment of H_2L ligand in **CuL-1**.

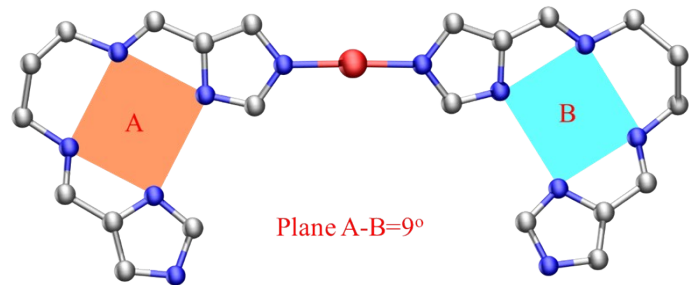


Fig. S4 The coordination environment of Cu(I) in **CuL-1**.

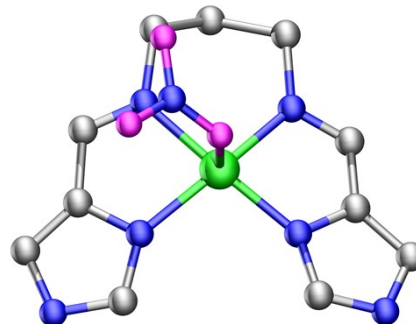


Fig. S5 The coordination environment of Cu(II) in **CuL-1**.

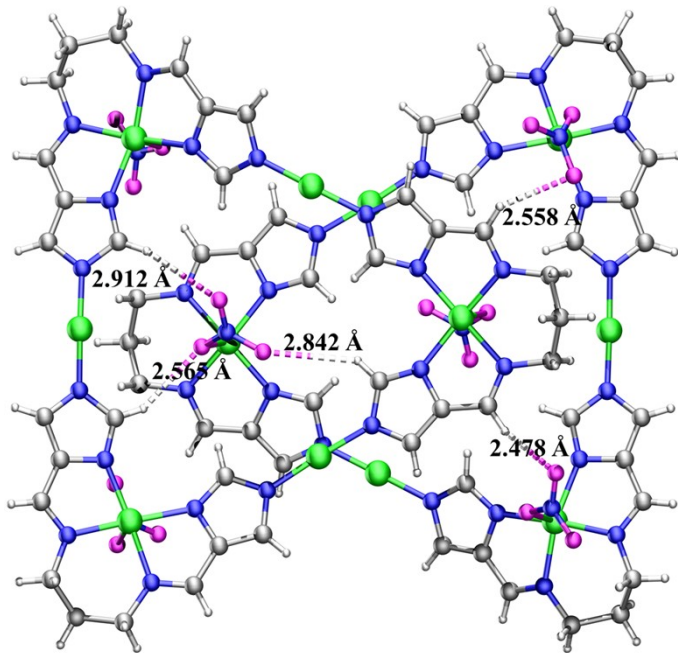


Fig. S6 The week C—H⋯O interactions between adjacent molecules of **CuL-1** and the H⋯O bond distance is 2.478–2.912 Å.

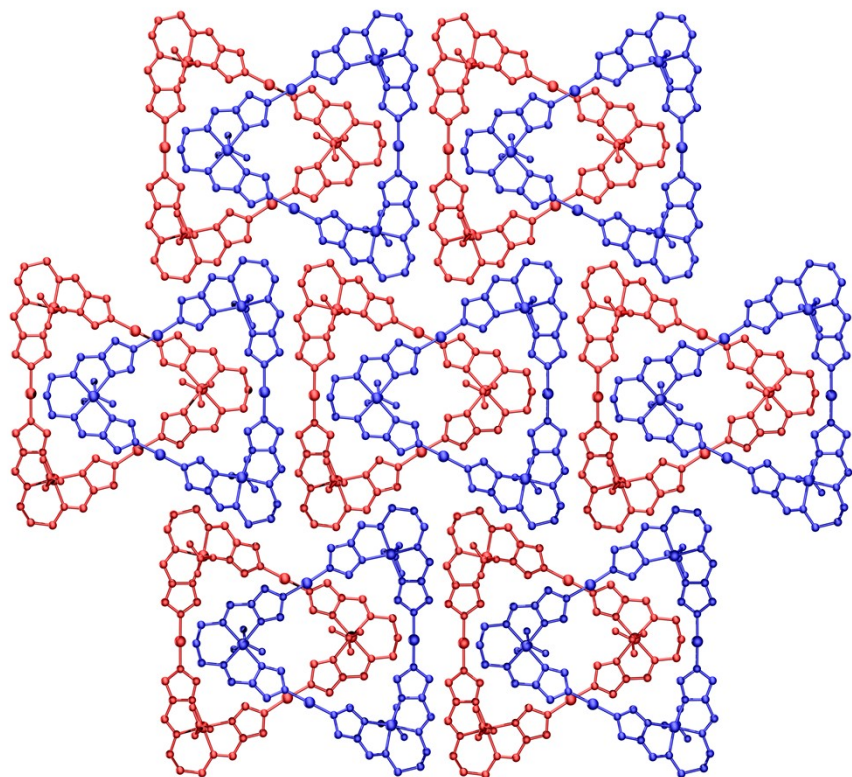


Fig. S7 The packing diagram of **CuL-1**.

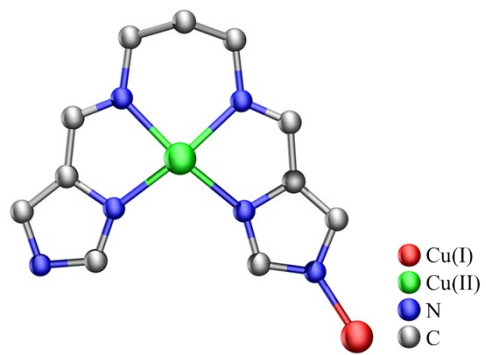


Fig. S8 The asymmetric unit of **CuL-2**, **CuL-3**, and **CuL-4**. All hydrogen atoms are omitted for clarity.

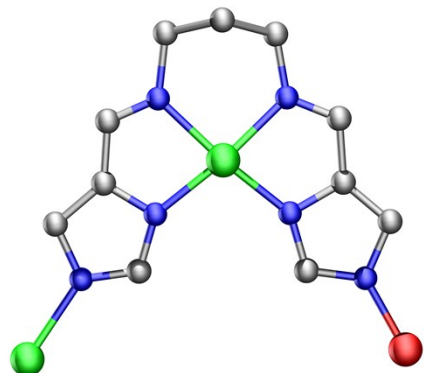


Fig. S9 The coordination environment of H_2L ligand in **CuL-2**, **CuL-3**, and **CuL-4**.

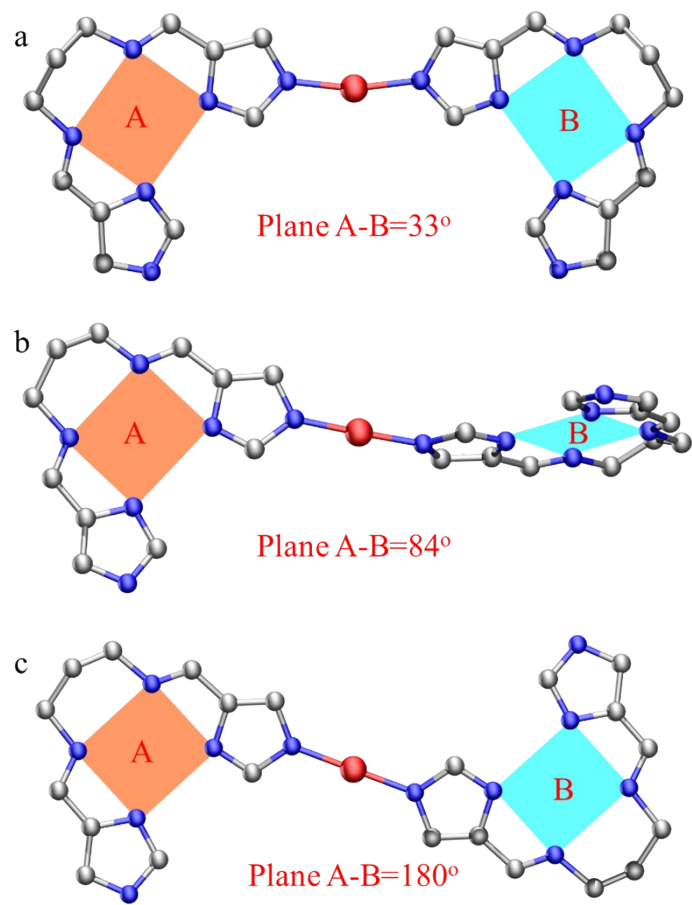


Fig. S10 The coordination environment of Cu(I) ion in (a) CuL-2, (b) CuL-3, and (c) CuL-4.

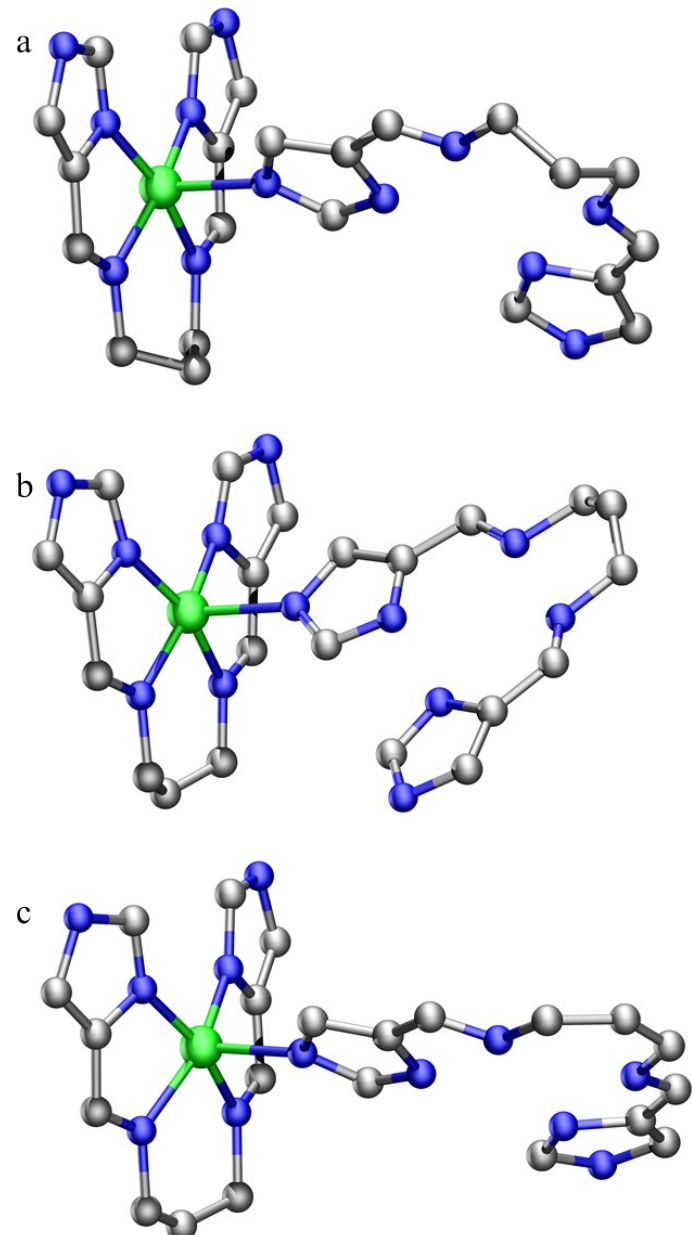


Fig. S11 The coordination environment of Cu(II) ion in (a) **CuL-2**, (b) **CuL-3**, and (c) **CuL-4**.

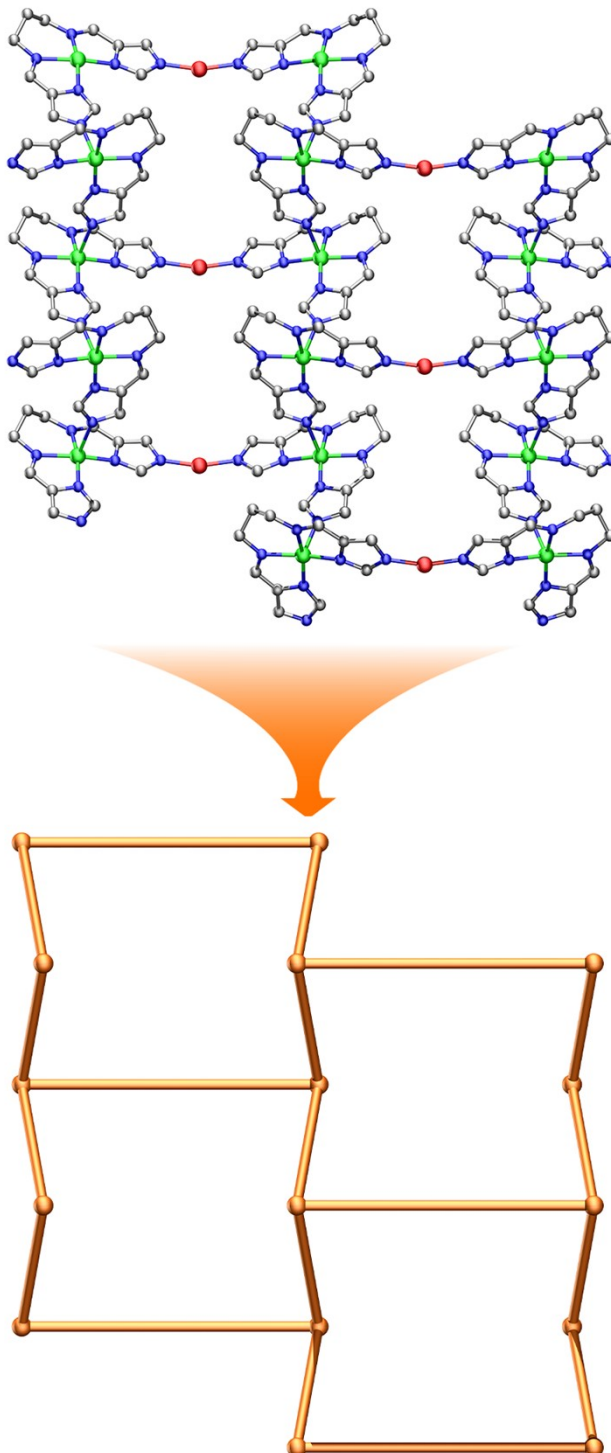


Fig. S12 The single layer and responding *hcb* topos of **CuL-2**.

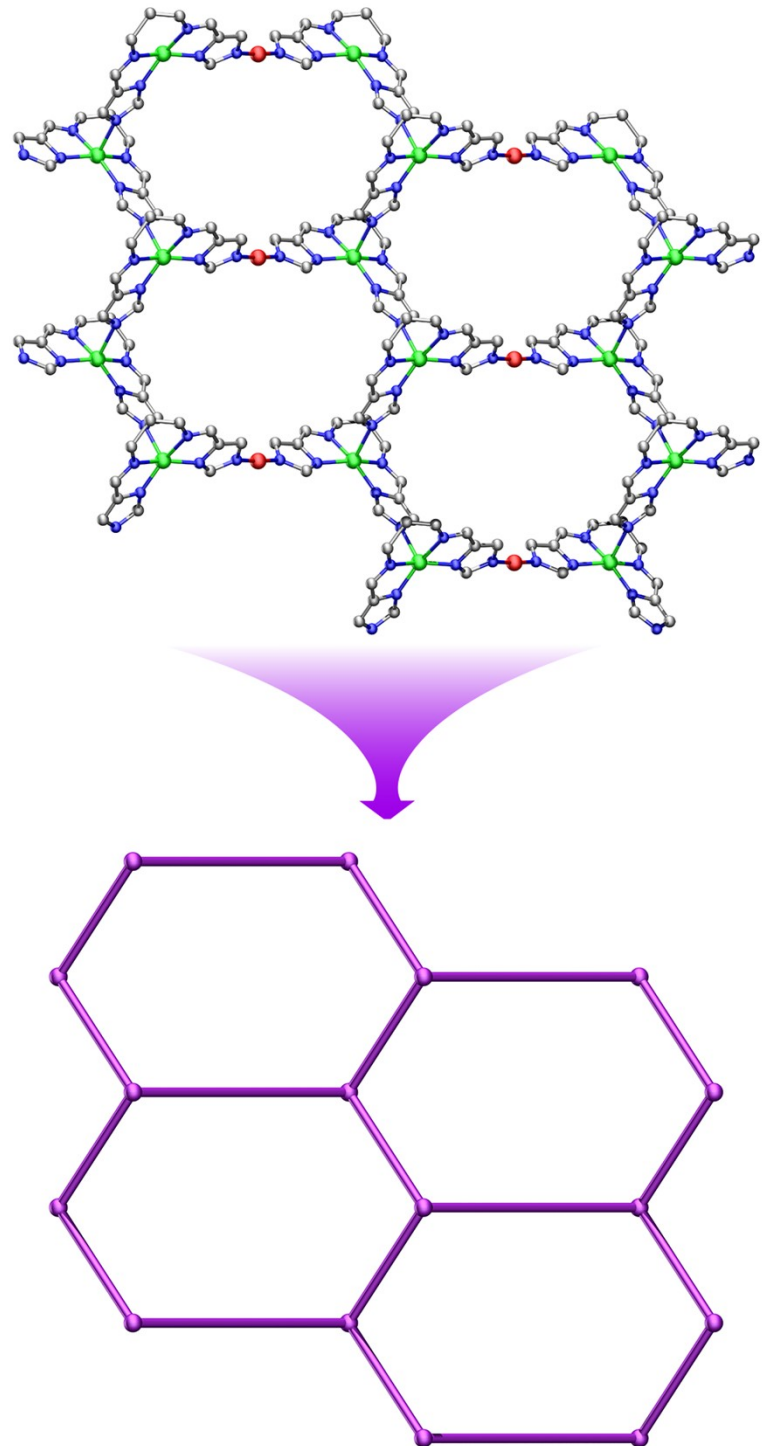


Fig. S13 The single layer and responding *hcb* topos of **CuL-3**.

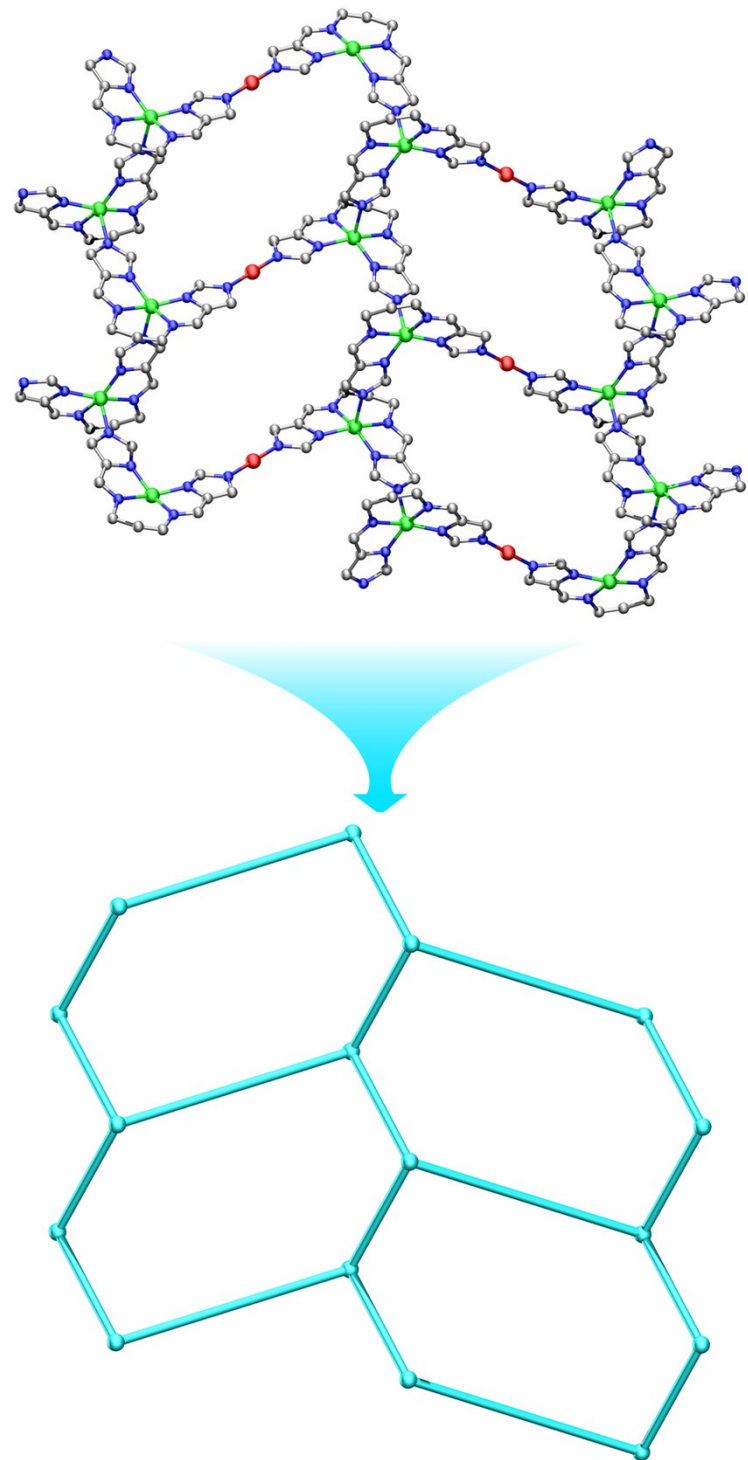


Fig. S14 The single layer and responding *hcb* topos of CuL-4.

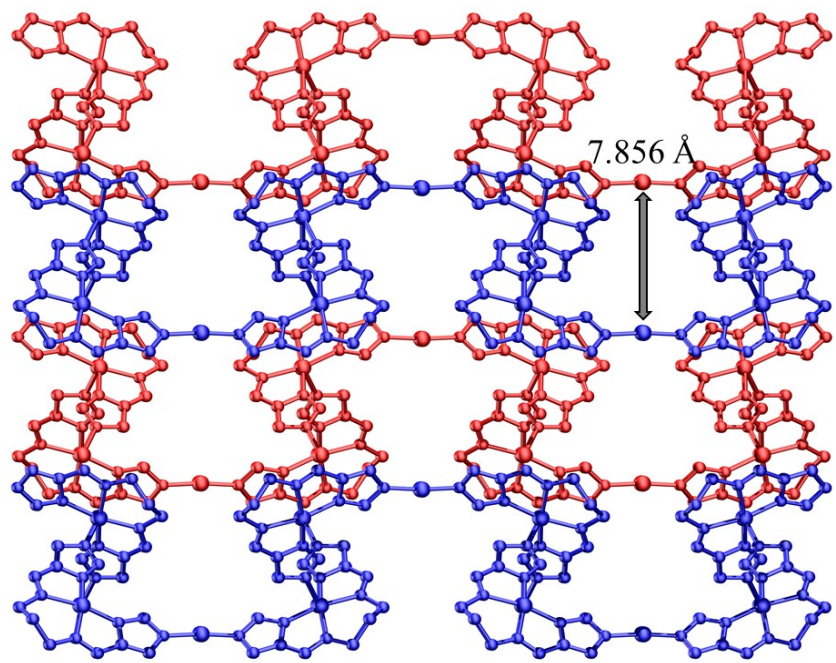


Fig. S15 The packing diagram of **CuL-2** and the layer spacing is 7.856 Å.

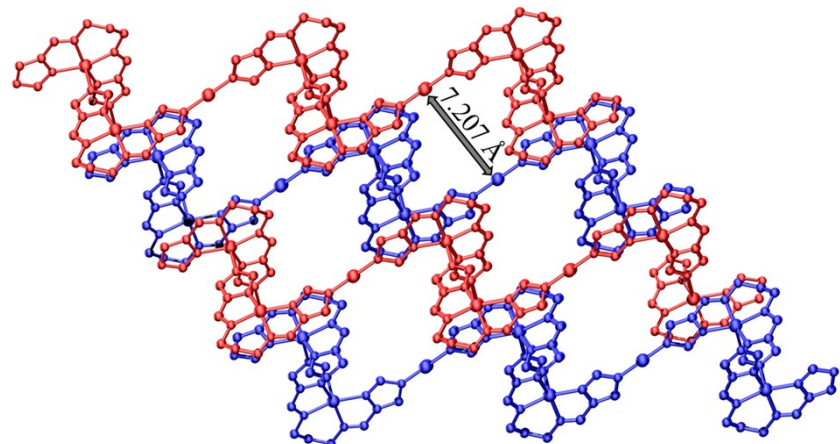


Fig. S16 The packing diagram of **CuL-3** and the layer spacing is 7.207 Å.

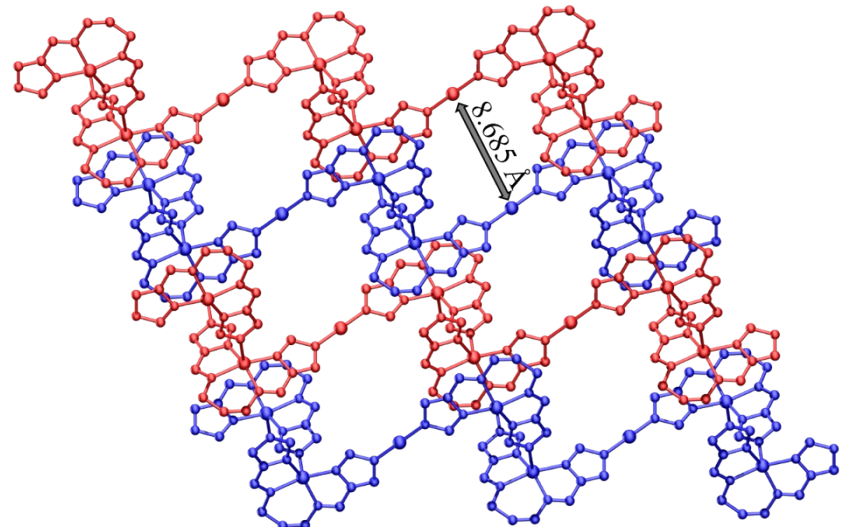


Fig. S17 The packing diagram of **CuL-4** and the layer spacing is 8.685 Å.

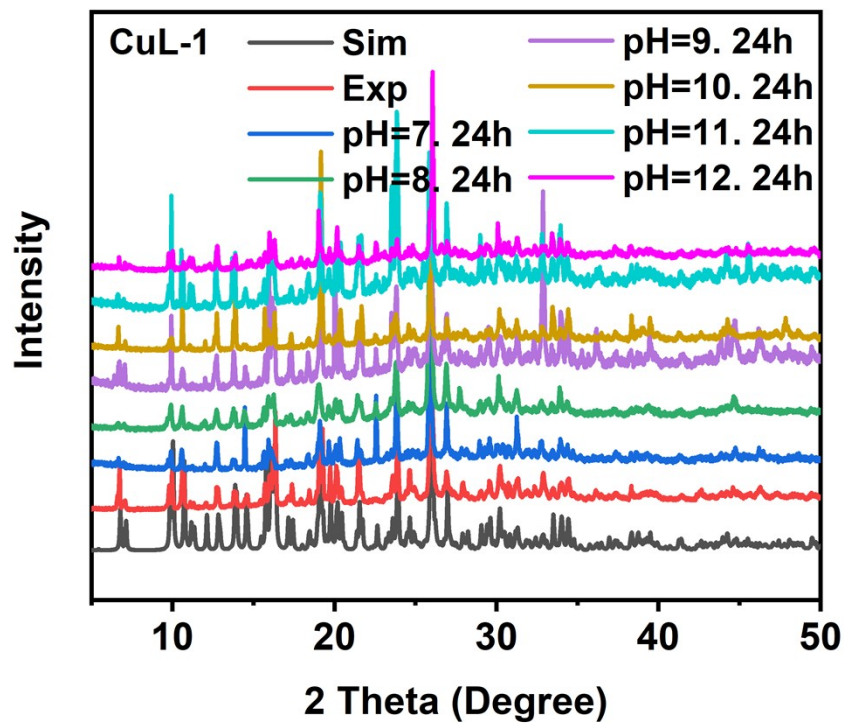


Fig. S18 PXRD patterns of CuL-1.

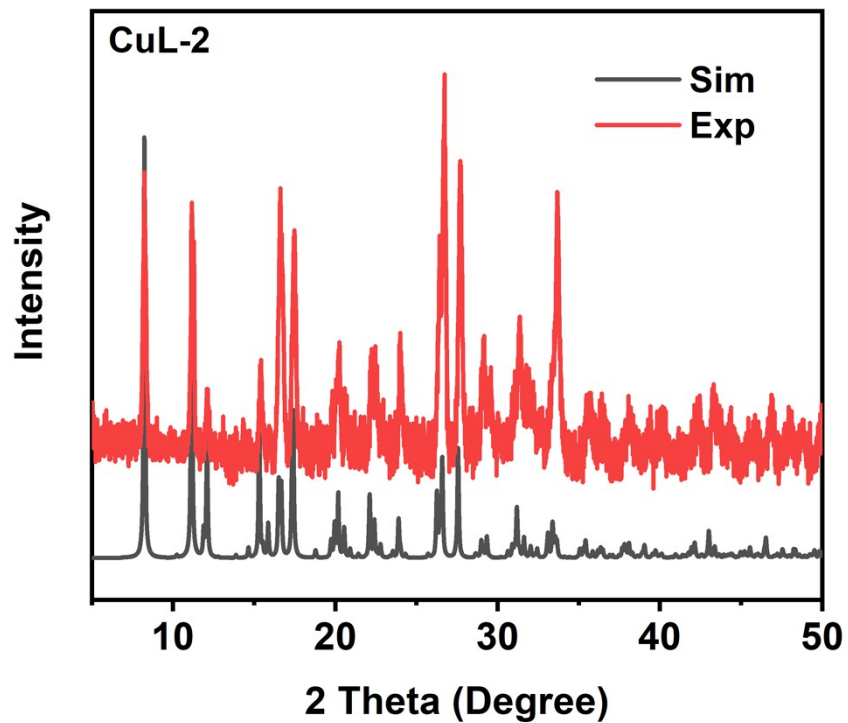


Fig. S19 PXRD patterns of CuL-2.

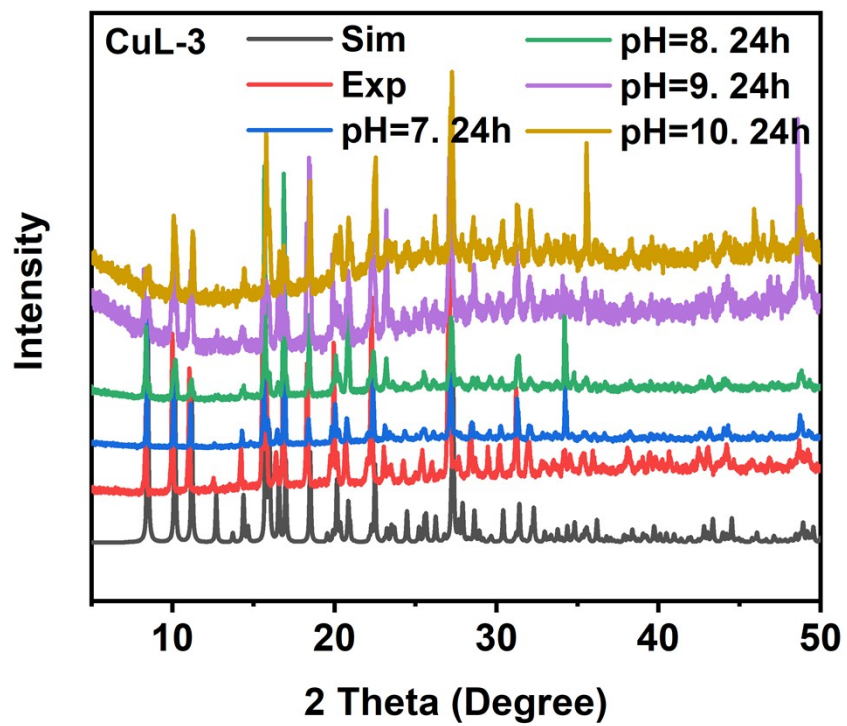


Fig. S20 PXRD patterns of CuL-3.

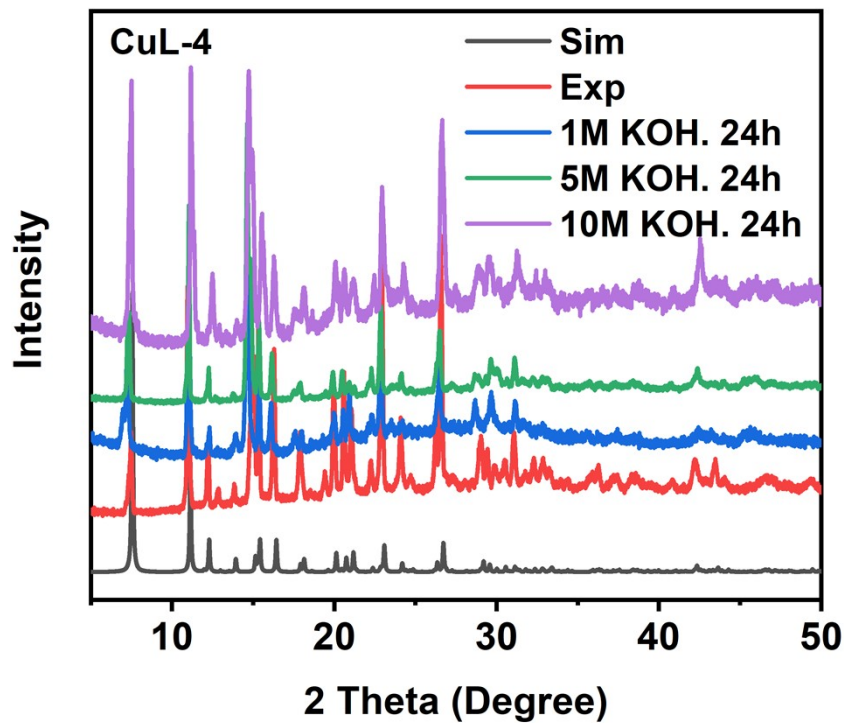


Fig. S21 PXRD patterns of CuL-4.

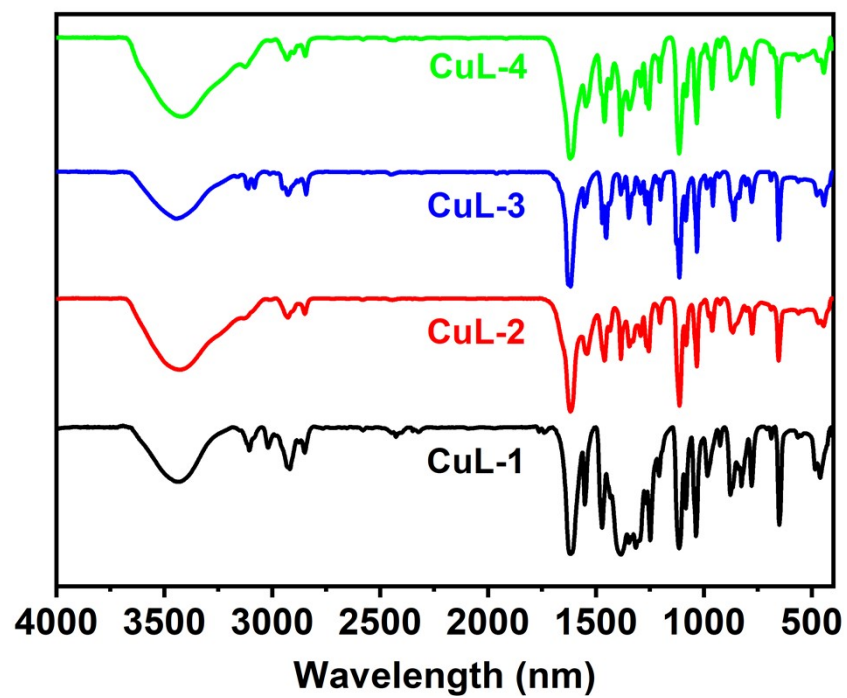


Fig. S22 The FT-IR spectra for **CuL-1**, **CuL-2**, **CuL-3**, and **CuL-4**.

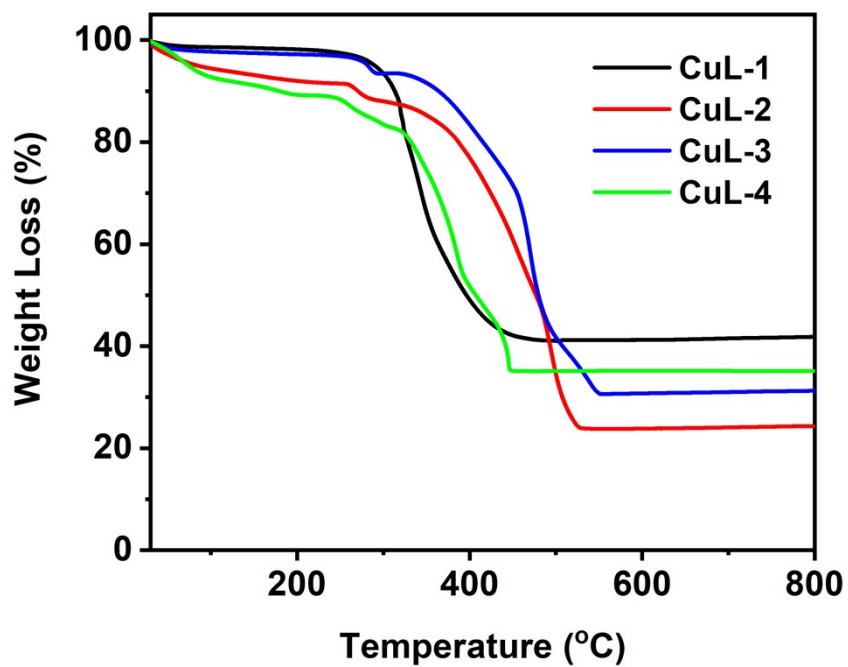


Fig. S23 Thermogravimetric analysis of CuL-1, CuL-2, CuL-3, and CuL-4.

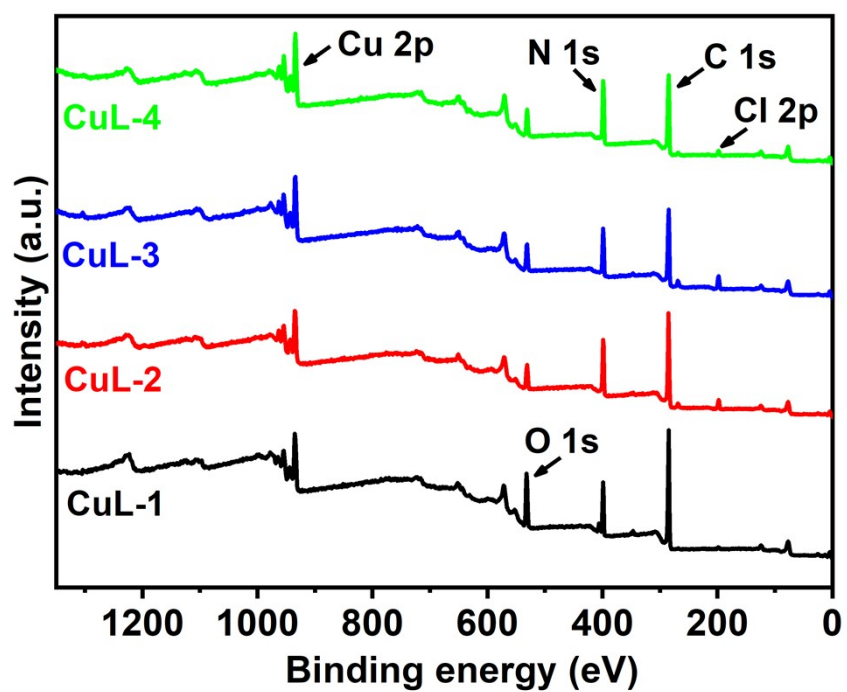


Fig. S24 The survey XPS spectra of CuL-1, CuL-2, CuL-3, and CuL-4.

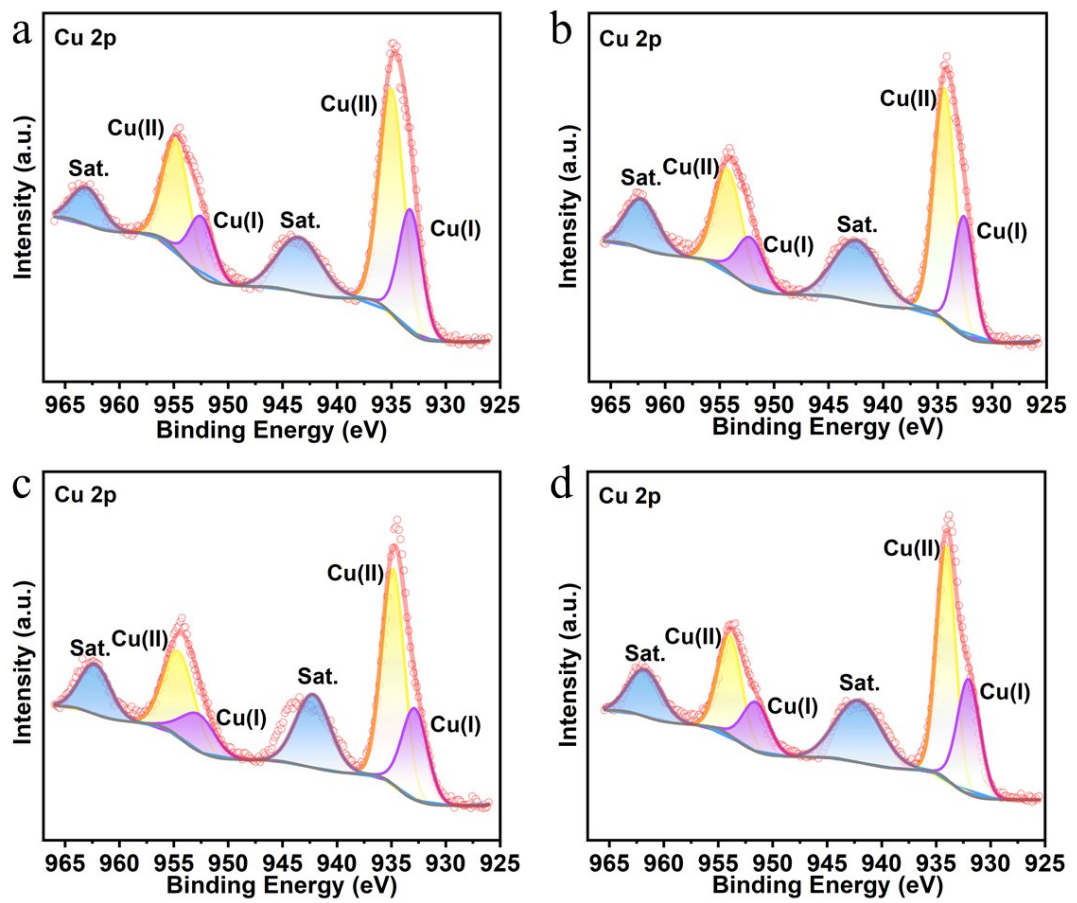


Fig. S25 The Cu 2p XPS spectra of (a) CuL-1, (b) CuL-2, (c) CuL-3, and (4) CuL-4.

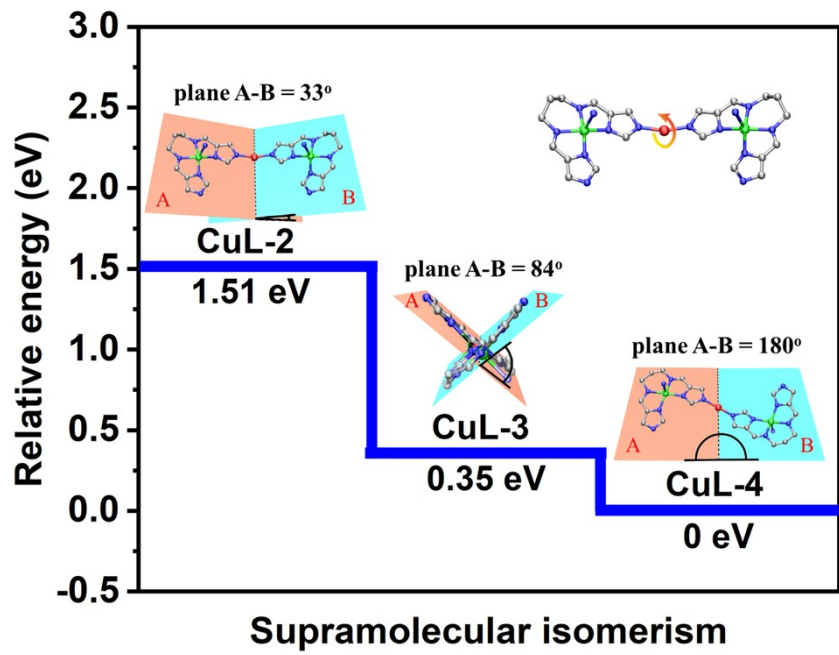


Fig. S26 DFT calculation of relative energy about CuL-2, CuL-3, and CuL-4.

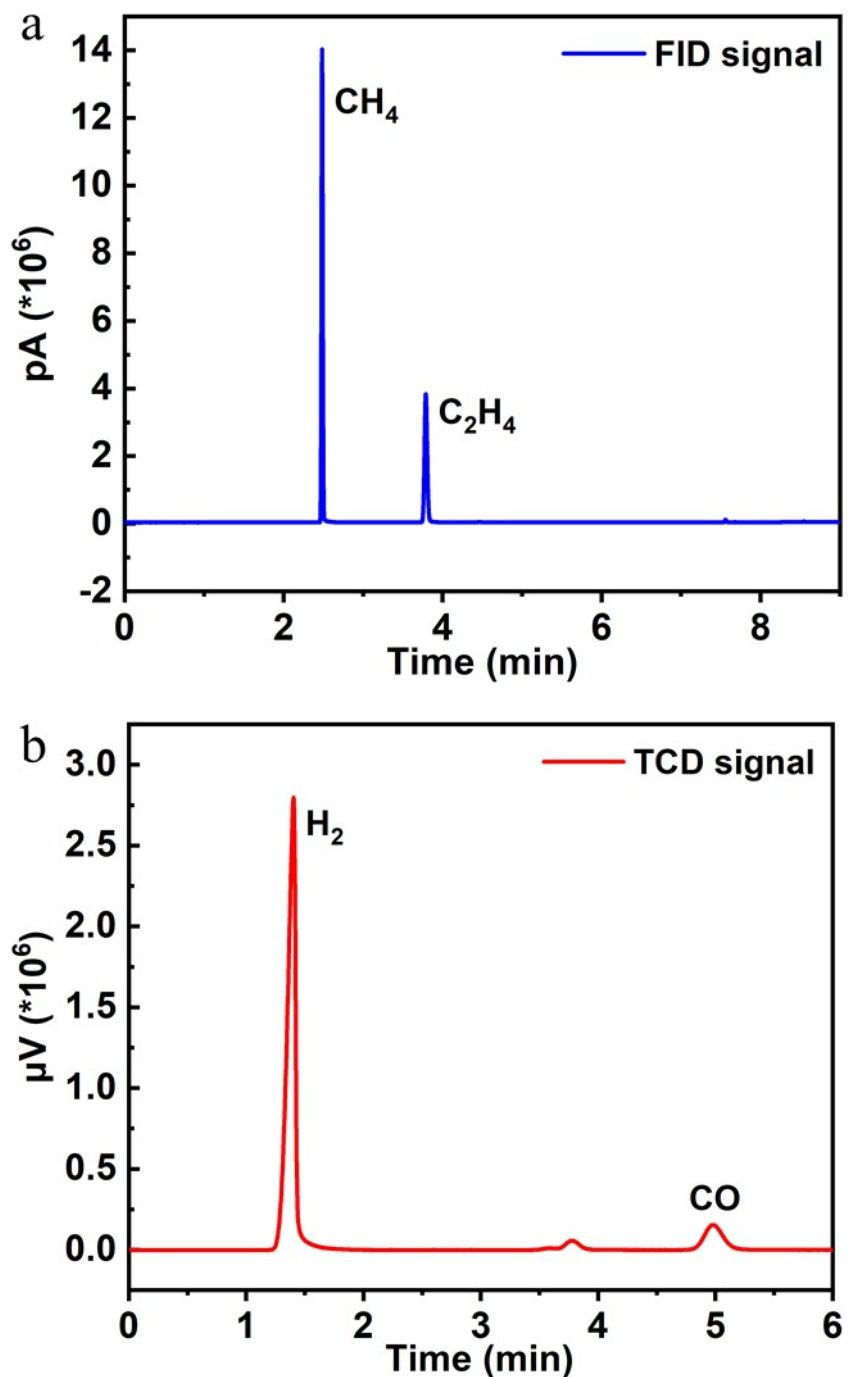


Fig. S27 GC spectrum of the gas products after electrocatalytic CO₂RR for 200 s at -1.0 V (vs. RHE) along with **CuL-4** as catalyst.

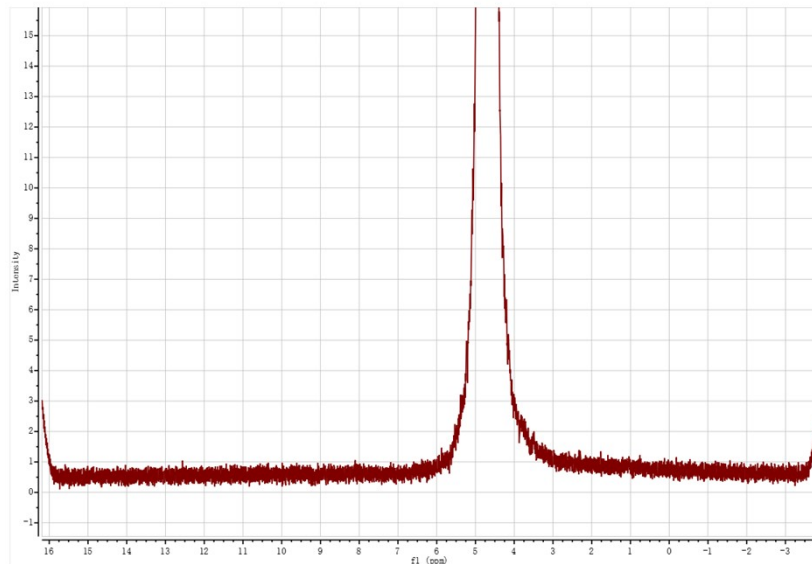


Fig. S28 ^1H NMR spectrum of the filtrate after electrocatalytic CO_2RR for 1 hour at -1.0 V (vs. RHE) using 50 mL 1 M KOH electrolyte along with **CuL-4** as catalyst.

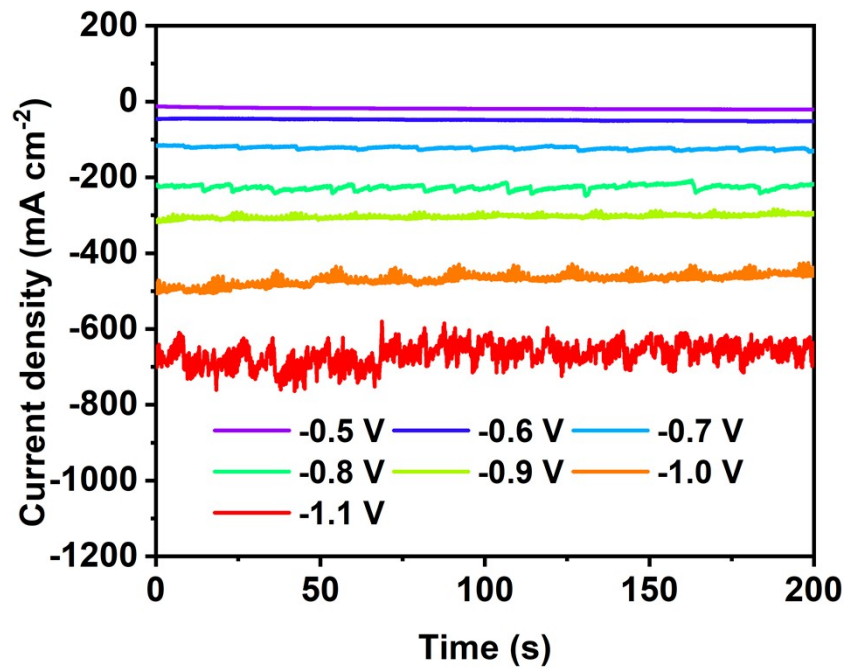


Fig. S29 Chronoamperometric curves at different applied potentials.

Table S10 The detail values of faradic efficiency catalyzed by CuL-4.

E(V vs. RHE)	H ₂ (%)	CO (%)	CH ₄ (%)	C ₂ H ₄ (%)	hydrocarbon s (%)	CO ₂ RR (%)
-0.5	75.37±3.77	17.27±0.75	0.80±0.03	0.37±0.01	1.16±0.04	18.43±0.71
-0.6	30.12±3.03	57.46±3.26	3.71±0.97	9.49±1.29	13.20±0.32	70.65±3.57
-0.7	11.19±2.03	36.21±0.15	14.67±0.05	31.85±1.78	46.53±1.83	82.73±1.69
-0.8	8.65±0.25	22.79±4.04	39.81±5.17	24.88±5.87	64.69±0.69	87.48±0.73
-0.9	10.19±0.41	6.31±0.80	58.17±4.61	23.28±6.48	81.45±1.87	87.76±2.66
-1.0	7.75±2.84	4.89±1.00	67.76±4.42	17.26±4.92	85.02±0.51	89.90±1.10
-1.1	17.82±1.49	2.64±0.59	62.93±5.11	18.25±6.85	81.19±1.74	83.82±2.32

Table S11 The performance of different crystalline electrocatalysts and their related products in CO₂RR.

Catalysts	Main product	Faradic efficiency (%)	Potential	Current density (mA cm ⁻²)	References
CuL-4	CH ₄	67.76	-1.0 V vs. RHE	477.42	This work
NNU-15	CO	99.2	-0.6 V vs. RHE	2.7	10
Co-PMOF	CO	98.7	-0.8 V vs. RHE	18.08	11
Re-SURMOF	CO	93±5	-1.6 V vs. NHE	2.5	12
ZIF-A-LD	CO	90.57	-1.1 V vs. RHE	/	13
ZIF-90-4	CO	90	-0.97 V vs. RHE	12.85	14
Ag ₂ O/layered ZIF	CO	80.6	-1.2 V vs. RHE	26.2	15
Al ₂ (OH) ₂ TCPP-Co	CO	76	-0.7 V vs. RHE	/	16
ZIF-8	CO	65.5	-1.8 V vs. SCE	/	17
Fe_MOF-525	CO	41±8	-1.3 V vs. NHE	5.9	18
CR-MOF	HCOOH	98	-1.2 V vs. SHE	/	19
Bi MOF	HCOOH	95.5	-0.86 V vs. RHE	-11.2	20
Cu ₂ (L)-e/Cu	HCOOH	90.5	-1.80 V vs. Ag/Ag ⁺	65.8	21
Cu@MOF	HCOOH	28	-0.82 V vs. RHE	-1.2	22
Zn-BTC MOF/CP	CH ₄	88.3±3.8	-2.2 V vs. Ag/Ag ⁺	0.5±0.2	23
NNU-33(H)	CH ₄	82	-0.9 V vs. RHE	391	24
Cu ₂ O@Cu-MOF	CH ₄	63.2	-1.71 V vs. RHE	8.4	25

Cu30%ZIF-8	CH ₄	35	-1.6 V vs. Ag/Ag+	NA	26
RE-ndc-fcu- MOF @AuNMEs	CH ₄	0.5±0.1	-0.5 V vs. RHE	-2.5	27
Cu ₃ (HHTQ) ₂	CH ₃ OH	53.6	-0.4 V vs. RHE	-0.5	28
HKUST-1 (Cu, Ru)	C ₂ H ₅ OH, CH ₃ OH	47.2	NA	20	29

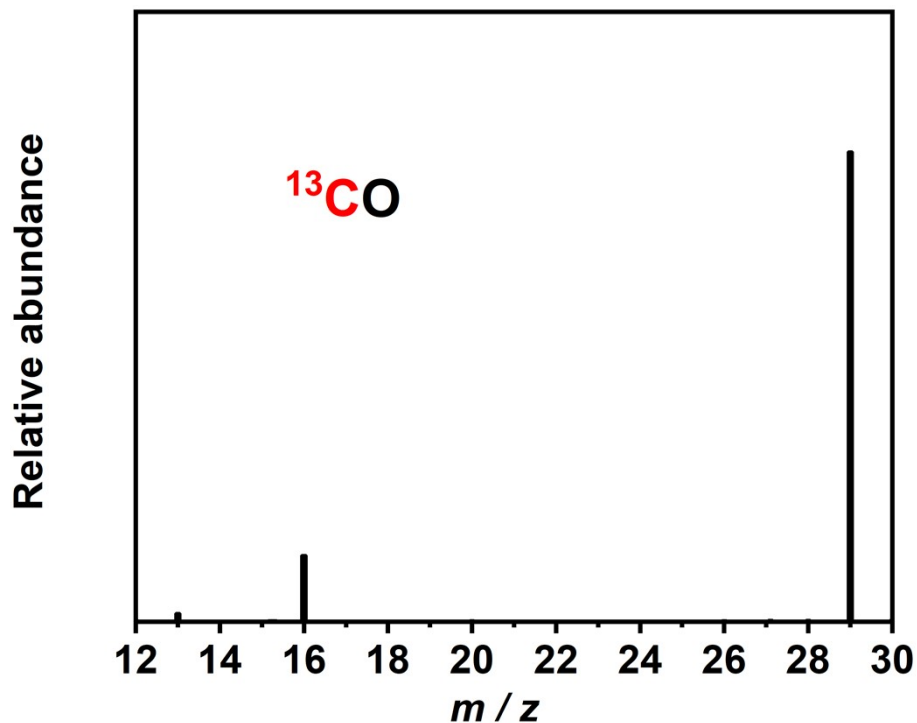


Fig. S30 Mass spectra extracted from GC-MS analysis of ¹³CO product from ¹³CO₂ reduction.

For the reduction of CO₂ to CH₄ (Fig. 3e), the peaks at *m/z* = 17, 16, 15, 14, 13 are assigned to ¹³CH₄, ¹³CH₃, ¹³CH₂, ¹³CH, ¹³C, respectively. For the reduction of CO₂ to C₂H₄ (Fig. 3f), the peaks at *m/z* = 30, 29, 28, 27, 26, 15, 14, 13 are assigned to ¹³C₂H₄, ¹³C₂H₃, ¹³C₂H₂, ¹³C₂H, ¹³C₂, ¹³CH₂, ¹³CH, ¹³C, respectively. For the reduction of CO₂ to CO (Fig. S30), the peaks at *m/z* = 29, 16, 13 are assigned to ¹³CO, O, ¹³C, respectively.

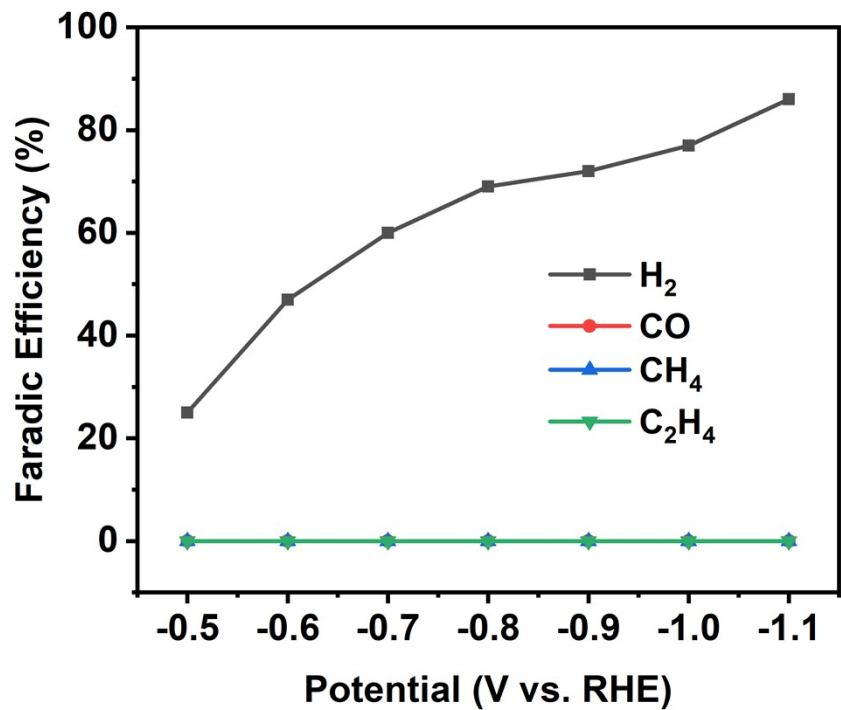


Fig. S31 Faradaic efficiencies for gaseous products of bare carbon paper at different applied potentials.

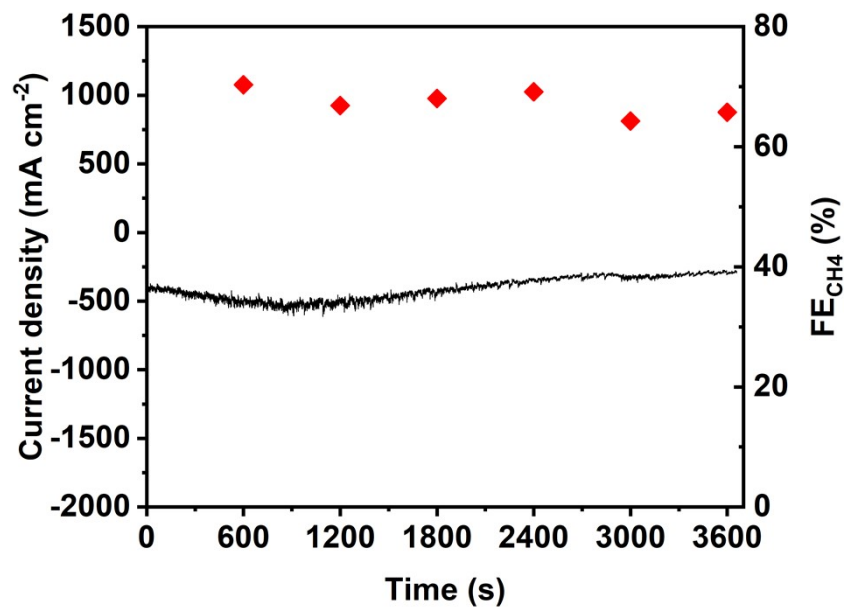


Fig. S32 The current profile and FEs of CH₄ at a constant voltage of -1.0 V vs. RHE.

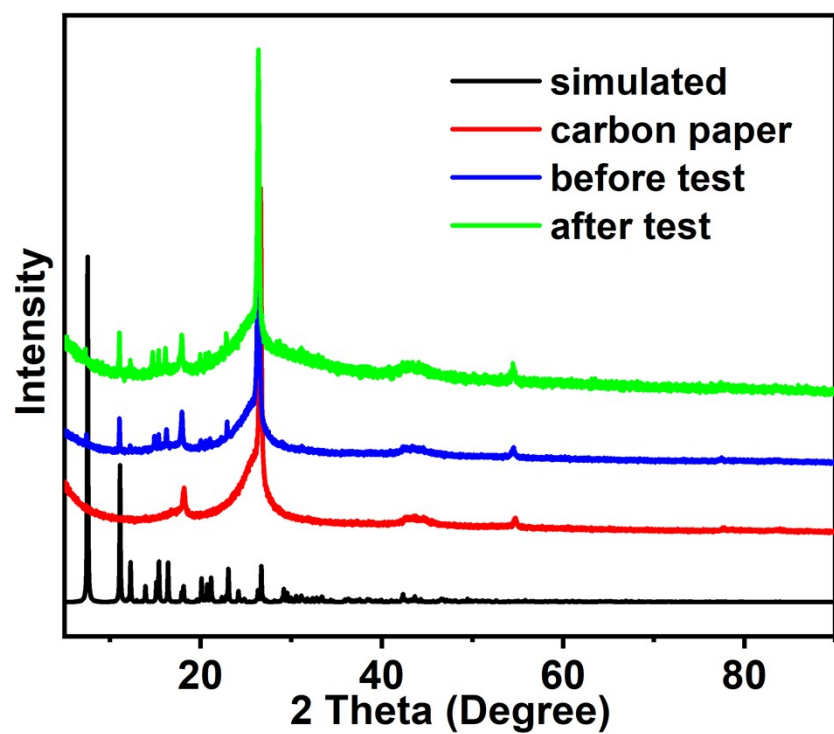


Fig. S33 PXRD patterns of CuL-4 before and after CO₂RR test. The carbon paper coated catalyst (1 mg cm⁻²) was directly used to test PXRD.

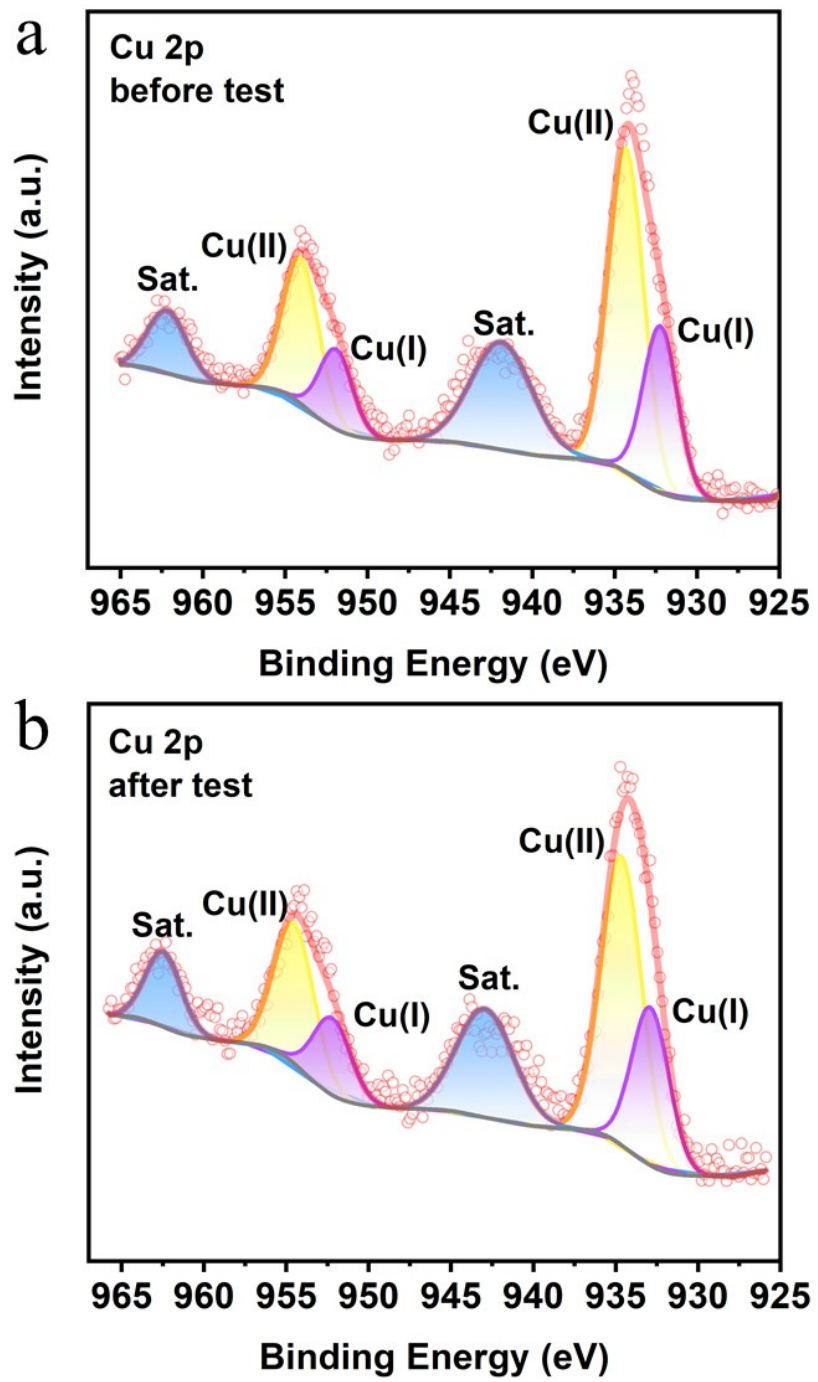


Fig. S34 Cu 2p XPS patterns of **CuL-4** before and after CO₂RR test. The carbon paper coated catalyst (1 mg cm⁻²) was directly used to test XPS.

As shown in Fig. S34a, before test, the Cu 2p_{3/2} peak can be divided into two components. Binding energy at 934.33 eV and 932.22 eV are belonged to Cu(II) and Cu(I) ions. And the deconvolution of the Cu 2p_{1/2} peak can be assigned to the Cu(II) (954.07 eV) and Cu(I) (951.92 eV), respectively. And the Cu 2p peaks after test (Fig. S34b) are similar as that before test. Binding energy at 934.53 eV (Cu 2p_{3/2}) and 954.25 eV (Cu 2p_{1/2}) are belonged to Cu(II) ions, while binding energy at 932.30 eV (Cu 2p_{3/2}) and 952.21 eV (Cu 2p_{1/2}) are belonged to Cu(I) ions.

Table S12 ICP and ICP-MS analysis of solution after electroreduction (-1.0 V) of CO₂ for **CuL-4**.

Electrolyte (after reaction)		µg L ⁻¹
ICP	Cu	< detection limit
ICP-MS	Cu	< detection limit

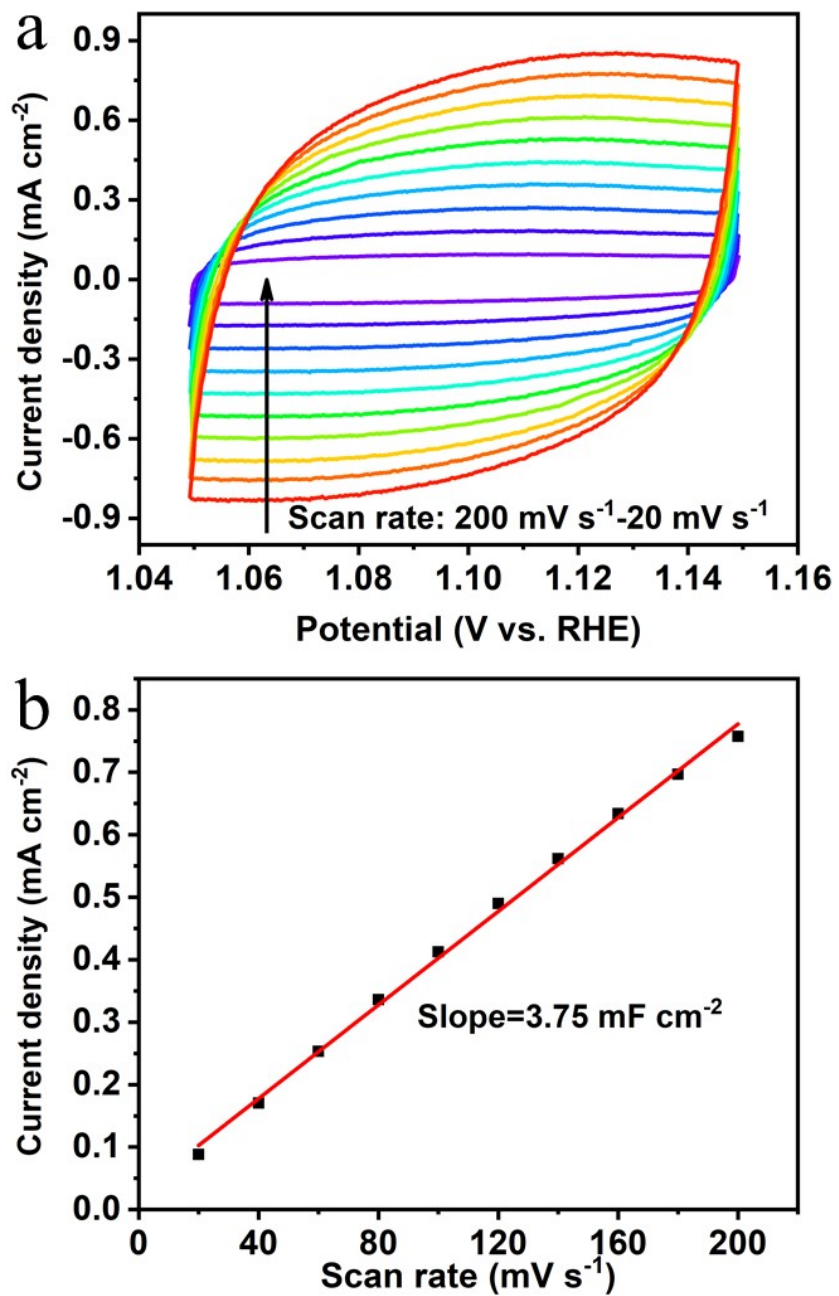


Fig. S35 Cyclic voltammetrys (CV) curves in the region of $1.05\text{-}1.15 \text{ V}$ vs. RHE at various scan rate ($20 \sim 200 \text{ mV s}^{-1}$) and corresponding capacitive current of **CuL-4**. And the C_{dl} of **CuL-4** is 3.75 mF cm^{-2}

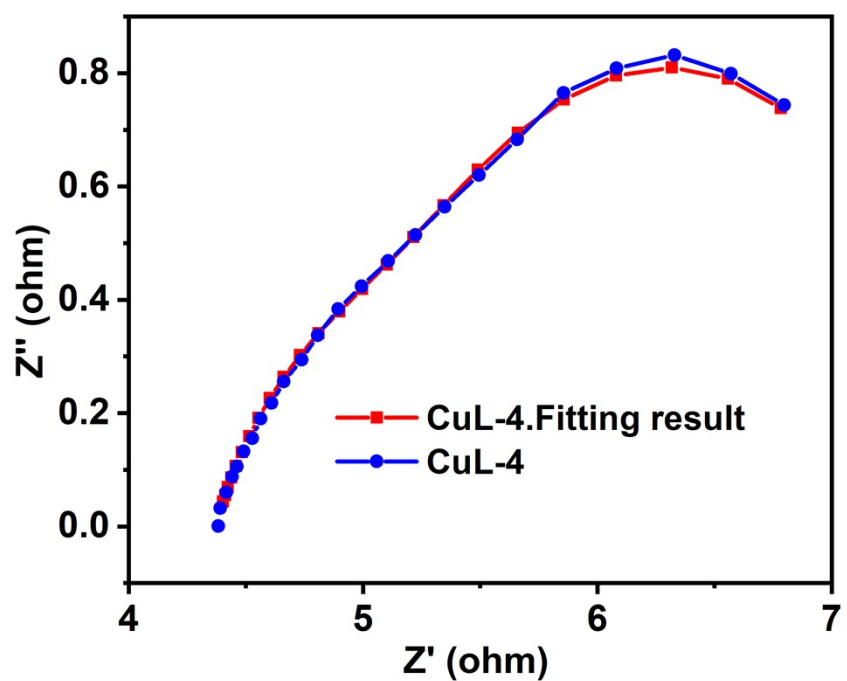


Fig. S36 The electrochemical impedance spectroscopy of **CuL-4** in 1 M KOH. And the charge transfer resistance (R_{ct}) of CuL-4 is 2.248 Ω .

Table S13 Free energies for elementary steps involved in CH₄ generation from CO₂ reduction on Cu(I) and Cu(II) sites of **CuL-4** at -1.0 V.

Elementary steps	ΔG (eV)	
	Cu(I) sites	Cu(II) sites
$^*\text{CO}_2^\bullet^- + \text{H}^+ + \text{e}^- \rightarrow ^*\text{COOH}$	-0.21	0.88
$^*\text{COOH} + \text{H}^+ + \text{e}^- \rightarrow ^*\text{CO} + \text{H}_2\text{O}(\text{l})$	0.36	-0.59
$^*\text{CO} + \text{H}^+ + \text{e}^- \rightarrow ^*\text{CHO}$	-0.08	0.29
$^*\text{CHO} + \text{H}^+ + \text{e}^- \rightarrow ^*\text{CHOH}$	0.53	0.71
$^*\text{CHOH} + \text{H}^+ + \text{e}^- \rightarrow ^*\text{CH} + \text{H}_2\text{O}(\text{l})$	-1.42	-1.55
$^*\text{CH} + \text{H}^+ + \text{e}^- \rightarrow ^*\text{CH}_2$	0.86	1.34
$^*\text{CH}_2 + \text{H}^+ + \text{e}^- \rightarrow ^*\text{CH}_3$	-2.16	-2.38
$^*\text{CH}_3 + \text{H}^+ + \text{e}^- \rightarrow \text{CH}_4(\text{g}) + ^*$	-0.78	-2.11

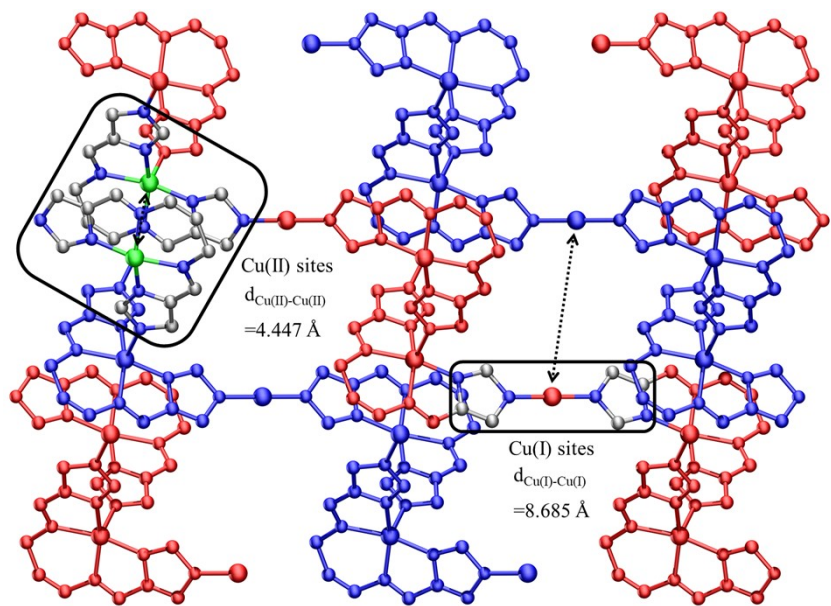


Fig. S37 The distance between adjacent two Cu(I) ions or two Cu(II) ions of CuL-4.

References

1. G. Kresse and J. Hafner, *Physical Review B*, 1993, **48**, 13115-13118.
2. G. Kresse and J. Furthmüller, *Physical Review B*, 1996, **54**, 11169-11186.
3. G. Kresse and J. Furthmüller, *Computational Materials Science*, 1996, **6**, 15-50.
4. J. P. Perdew, K. Burke and M. Ernzerhof, *Phys. Rev. Lett.*, 1996, **77**, 3865-3868.
5. P. E. Blöchl, *Physical Review B*, 1994, **50**, 17953-17979.
6. K. Mathew, V. S. C. Kolluru, S. Mula, S. N. Steinmann and R. G. Hennig, *The Journal of Chemical Physics*, 2019, **151**, 234101.
7. K. Mathew, R. Sundararaman, K. Letchworth-Weaver, T. A. Arias and R. G. Hennig, *The Journal of Chemical Physics*, 2014, **140**, 084106.
8. M. Van den Bossche, E. Skúlason, C. Rose-Petrucci and H. Jónsson, *J. Phys. Chem. C*, 2019, **123**, 4116-4124.
9. J. K. Nørskov, J. Rossmeisl, A. Logadottir, L. Lindqvist, J. R. Kitchin, T. Bligaard and H. Jónsson, *The Journal of Physical Chemistry B*, 2004, **108**, 17886-17892.
10. Q. Huang, Q. Li, J. Liu, Y. R. Wang, R. Wang, L. Z. Dong, Y. H. Xia, J. L. Wang and Y.-Q. Lan, *Matter*, 2019, **1**, 1656-1668.
11. Y.-R. Wang, Q. Huang, C.-T. He, Y. Chen, J. Liu, F.-C. Shen and Y.-Q. Lan, *Nat. Commun.*, 2018, **9**, 4466.
12. L. Ye, J. Liu, Y. Gao, C. Gong, M. Addicoat, T. Heine, C. Woell and L. Sun, *J. Mater. Chem. A*, 2016, **4**, 15320-15326.
13. S. Dou, J. Song, S. Xi, Y. Du, J. Wang, Z.-F. Huang, Z. J. Xu and X. Wang, *Angew. Chem. Int. Ed.*, 2019, **58**, 4041-4045.
14. Z. Yang, X. Zhang, C. Long, S. Yan, Y. Shi, J. Han, J. Zhang, P. An, L. Chang and Z. Tang, *CrystEngComm*, 2020, **22**, 1619-1624.
15. X. Jiang, H. Wu, S. Chang, R. Si, S. Miao, W. Huang, Y. Li, G. Wang and X. Bao, *J. Mater. Chem. A*, 2017, **5**, 19371-19377.
16. N. Kornienko, Y. Zhao, C. S. Kiley, C. Zhu, D. Kim, S. Lin, C. J. Chang, O. M. Yaghi and P. Yang, *J. Am. Chem. Soc.*, 2015, **137**, 14129-14135.
17. Y. Wang, P. Hou, Z. Wang and P. Kang, *ChemPhysChem*, 2017, **18**, 3142-3147.
18. I. Hod, M. D. Sampson, P. Deria, C. P. Kubiak, O. K. Farha and J. T. Hupp, *ACS Catal.*, 2015, **5**, 6302-6309.
19. R. Hinogami, S. Yotsuhashi, M. Deguchi, Y. Zenitani, H. Hashiba and Y. Yamada, *Ecs Electrochemistry Letters*, 2012, **1**, H17-H19.
20. X. Zhang, Y. Zhang, Q. Li, X. Zhou, Q. Li, J. Yi, Y. Liu and J. Zhang, *J. Mater. Chem. A*, 2020, **8**, 9776-9787.
21. X. Kang, L. Li, A. Sheveleva, X. Han, J. Li, L. Liu, F. Tuna, E. J. L. McInnes, B. Han, S. Yang and M. Schroeder, *Nat. Commun.*, 2020, **11**, 5464.
22. C.-W. Kung, C. O. Audu, A. W. Peters, H. Noh, O. K. Farha and J. T. Hupp, *ACS Energy Lett.*, 2017, **2**, 2394-2401.
23. X. Kang, Q. Zhu, X. Sun, J. Hu, J. Zhang, Z. Liu and B. Han, *Chem. Sci.*, 2016, **7**, 266-273.
24. L. Zhang, X.-X. Li, Z.-L. Lang, Y. Liu, J. Liu, L. Yuan, W.-Y. Lu, Y.-S. Xia, L.-Z. Dong, D.-Q. Yuan and Y.-Q. Lan, *J. Am. Chem. Soc.*, 2021, **143**, 3808-3816.
25. X. Y. Tan, C. Yu, C. T. Zhao, H. W. Huang, X. C. Yao, X. T. Han, W. Guo, S. Cui, H. L.

- Huang and J. S. Qiu, *ACS Appl. Mater. Interfaces*, 2019, **11**, 9904-9910.
26. A. Ahmad, N. Iqbal, T. Noor, A. Hassan, U. A. Khan, A. Wahab, M. A. Raza and S. Ashraf, *Journal of Co₂ Utilization*, 2021, **48**, 101523.
27. P. De Luna, W. Liang, A. Mallick, O. Shekhah, F. P. G. de Arquer, A. H. Proppe, P. Todorovic, S. O. Kelley, E. H. Sargent and M. Eddaoudi, *ACS Appl. Mater. Interfaces*, 2018, **10**, 31225-31232.
28. J. Liu, D. Yang, Y. Zhou, G. Zhang, G. Xing, Y. Liu, Y. Ma, O. Terasaki, S. Yang and L. Chen, *Angewandte Chemie-International Edition*, 2021, **60**, 14473-14479.
29. M. Perfecto-Irigaray, J. Albo, G. Beobide, O. Castillo, A. Irabien and S. Perez-Yanez, *Rsc Advances*, 2018, **8**, 21092-21099.